Tarjei Nygaard Skulstad

# High Performance Valve Spring Failure Mode Detection

Master's thesis in Mechanical Engineering
Supervisor: Terje Rølvåg
June 2019

Master's thesis

NTNU
Norwegian University of Science and Technology
Faculty of Engineering
Department of Mechanical and Industrial Engineering

NTNU
Kunnskap for en bedre verden

Tarjei Nygaard Skulstad

# High Performance Valve Spring Failure Mode Detection

Master's thesis in Mechanical Engineering
Supervisor: Terje Rølvåg
June 2019

Norwegian University of Science and Technology
Faculty of Engineering
Department of Mechanical and Industrial Engineering

NTNU
Norwegian University of
Science and Technology

# Summary

In this paper, it is evaluated how a valve train controls the operation of the valves, specifically how the cam profile and rocker arm setup interacts in order to generate a lift curve for the valves. It is studied how the shape of this curve influence power, torque and emissions for internal combustion engines. Multiple simulations of the exhaust valve springs of the Honda CRF250R 2018 model is performed for the purpose of evaluating whether the acceleration levels generated by the camshaft can initiate resonance problems and self-contact in the valve springs. A nonlinear static analysis is conducted so that the generated stress levels in the spring coils during operation can be investigated. Finally, the results are used in order to investigate whether fatigue could be a possible problem in the springs of the 2018 Honda CRF 250R.

# Sammendrag

I denne oppgaven blir det undersøkt hvordan ventilmekanismen i en forbrenningsmotor styrer ventilene, og da spesielt med tanke på hvordan kamprofilen og vippearmenes oppsett samvirker for å generere løftkurven for ventilene. Det undersøkes hvordan formen på denne kurven påvirker kraft, dreiemoment og utslipp for forbrenningsmotorer. Flere simuleringer av eksosventilfjærene i 2018 modellen av Honda CRF250R utføres for å vurdere om akselerasjonsnivåene som genereres av kamakselen kan initiere resonansproblemer og selvkontakt i ventilfjærene. En ikke-lineær statisk analyse utføres for å undersøke de genererte spenningsnivåene som oppstår i ventilfjæren under drift. Til slutt brukes resultatene for å undersøke om utmattelse kan være et mulig problem i eksosfjærene til 2018 modellen av Honda CRF 250R.

# Preface

This master thesis was written at the Department of Mechanical and Industrial Engineering (NTNU), in the spring of 2019. In this paper Siemens NX is used to design and model central parts of the valvetrain of the Honda CRF250R 2018 model. This includes the valve springs, valves and retainers, cam shaft and rocker arms. The integrated NX Nastran finite element analysis program is used to perform a nonlinear static analysis of the exhaust valve spring during compression. The FEDEM software is used in order to conduct a dynamic analysis, and finally fatigue analyses of the valve train during load is performed in order to estimate the fatigue life of the valve springs.

# Contents

# List of Tables

# List of Figures

# Abbreviations

**ABDC** After Bottom Dead Center

**ATDC** After Top Dead Center

**BBDC** Before Bottom Dead Center

**BDC** Bottom Dead Centre

**CA** Crankshaft Angle

**CAD** Computer Aided Design

**CAE** Computer Aided Engineering

**CAM** Computer Aided Manufacturing

**CD** Discharge Coefficient

**CMS** Component Mode Synthesis

**CO** Carbon monoxide

**DOF** Degree of freedom

**DOHC** Dual Overhead Camshaft

**EC** Exhaust valve Closes

**EGR** Exhaust Gas Recirculation

**EO** Exhaust valve Opens

**FE** Finite Element

**FEA** Finite Element Analysis

**FEM** Finite Element Method

**IC** Inlet valve Closes

**IO** Inlet valve Opens

**IVC** Intake Valve Closing

**NURBS** Non Uniform Rational B-splines

**RBE2** Rigid Body Element, Form 2

**RPM** Revolutions Per Minute

**SEM** Scanning Electron Microscope

**SFC** Specific Fuel Consumption

**SI** Spark-igniton

**TDC** Top Dead Centre

**UTS** Ultimate Tensile Strength

Chapter 1

# Introduction

## 1.1 Background

Over the last years, racing engines have had the need to improve performance and reduce emissions. In order to achieve these goals, the design of the engine have become increasingly more refined. One effective way of maximising the power output of the engine is to optimise the air and fuel flow to the cylinder. This can be done by adjusting the cam profile and the rocker arm. The shape of the cam lobe, and the gearing from the rocker arm, directly affects the way the valves are operated. Therefore the design of these parts are crucial for the engine performance. In the engine of the 2018 Honda CRF250R, both the valve diameters, and the lift of the valves, are increased from the previous model in order to improve the air and fuel flow to the cylinder. The lift is increased from 9.2mm to 10.5mm for the intake valves, and 8.4 to 9.5mm for the exhaust valves. An increase in lift of more than $10\%$ for both of the valves. [Honda Motor Company (2018)]

Recently Honda have experienced some catastrophic engine failures on the 2018 model of the CRF250R. It is expected that these failures happens as a result of the valve springs at the exhaust valves fracturing during high Revolutions Per Minute (RPM), something that prevents the valve from closing properly, resulting in an obstruction of the piston. There is reason to believe that this problem has occurred as a result of the increased lift and it is therefore necessary to investigate how the exhaust valve springs behave during load. This paper is a collaboration between the Norwegian University of Science and Technology (NTNU) and MX Real Racing (MXRR) in Italy.

## 1.2 Objective

The main objective of this masters thesis is to find the reason for failure in the high performance valve springs of the Honda CRF250R 2018 model. This thesis will be partly based on the results from the project paper ”High performance cam profile design and optimization” also written by the signatory. The goal of this project was to perform an initial modal analysis of the exhaust valve compression spring with variable pitch for the 2018 HONDA CRF250R, in order to estimate the excitation frequencies and check for potential resonance problems in the springs. These analyses were conducted only on the exhaust valve springs in simplified simulations using Siemens NX.

In order to perform a more accurate analysis, the additional parts of the top assembly, including the cam shaft, rocker arm and valve retainer, are modelled by the use of Computer Aided Design (CAD) utilising Siemens NX software. These parts are then used to conduct a dynamic analysis on the whole valve train assembly using the FEDEM analysis software. From this analysis it can be studied whether the cam profile generate acceleration levels that initiate resonance problems and self-contact in the exhaust valve springs. A nonlinear static analysis of the spring in question is also performed in Siemens NX in order to evaluate the stress levels in the spring. Finally it is evaluated whether fatigue in the spring coils could be a problem, and the fatigue life of the springs are estimated.

In order to increase the power output of the engine in the 2018 model of the Honda CRF 250R, both the cam profiles and rocker arms are changed from previous models. These parts are directly controlling the lift curve. For that reason, some basic theory on how this curve influence power, torque and emissions for internal combustion engines is included.

Chapter 2

# Literature Review

This literature review is in part taken from the semester project ”High performance cam profile design and optimization” written in the fall 2018 by the signatory. As the main part of the task remains the same, all of the studies in that review are still considered relevant for this master thesis. Some additional papers, mainly concerning fatigue failures in valve springs, are also added.

## 2.1 Geehan and Ryason (2000)

A study conducted by Geehan and Ryason (2000) is looking into how it is possible to reduce the NOx emissions by controlling the valve timing. It concludes that reducing peak combustion temperatures is a possible approach to control NOx. This can be done by retarding fuel injection timing which then lowers peak combustion flame temperatures and reduces NOx formation by displacing the combustion event until later in the expansion stroke. This utilises the mechanical expansion of combustion volume to offset increases in pressure and temperature.

## 2.2 Sahu et al. (2016)

Sahu et al. (2016) reviews earlier research work in the field of kinematic and dynamic aspects of design and optimisation of cam profiles for high performance machinery demands. They conclude that splines are increasingly replacing polynomials as the mathematical representation of cam profiles because of their versatility, ease of application and flexibility.

This is made possible by the advances in computer science over the last decades. Also, they conclude that curves like Bezier and Non Uniform Rational B-splines (NURBS) can help when it comes to increasing the accuracy of the cam profile.

## 2.3 CARDONA et al. (2002)

In this research paper a design methodology is establishes in order to design cams using a constrained optimisation algorithm. The algorithm is designed to optimise valve lift and timings of the valves in order to maximise the time integral of the valve area opened to gas flow. This is important as the flow field within the cylinder is the most crucial factor controlling the combustion and engine breathing processes. An increase in the valve lift and the time interval of the valve operation does not necessarily lead to an expanded gas flow, as other factors also influence the effective flow. This is due to other phenomena that has to be taken into account. The most important of these are the Discharge Coefficient (CD) which defines an effective flow area. Finally, the valve lift and timings are important for the turbulence inside the combustion chamber. This will influence the combustion process and consequently the thermal efficiency of the engine. In the analysis of the Honda CRF250R 2018 model, this paper is found useful as expanded gas flow, achieved by increasing the lift of the valves, is one of the main improvements compared to previous models. After an optimal lift curve is established, CARDONA et al. (2002) compute the cam shape using inverse kinematics.

## 2.4 Rui-Ming et al. (2013)

Rui-Ming et al. (2013) proposes a method of designing cam curves based on classical splines. A universal method of calculating the desired cam shape in order to satisfy given boundary conditions and specific requirements is discussed. It is shown that by using splines, it is possible to locally change the cam curve in order to adjust acceleration or jerk of the camshaft, without influencing the overall design constraints.

## 2.5 CINAR and AKGUN (2007)

This study by ÇINAR and AKGÜN (2007) is especially relevant when it comes to determining the optimal design of the camshaft in order to control the exhaust valve so that given parameters can be maximised. In the study a special variable control mechanism is designed and manufactured in order to control the Intake Valve Closing (IVC) time. The IVC time was varied between a Crankshaft Angle (CA) of 38°After Bottom Dead Center (ABDC) to 78°ABDC in four steps, where a CA of 48°was set as the standard timing.

Exhaust valve opening and closing time, intake valve opening time, and lift were not varied. A single cylinder, four stroke, Spark-igniton (SI) engine was used for the experiments. Depending on the engine speed, brake torque, volumetric efficiency and Specific Fuel Consumption (SFC), exhaust emission variations were investigated for different IVC time values.

The brake torque was increased by 5.1% at low engine speeds by advancing the IVC. Additionally, by retarding the IVC it was increased by 4.6% for high engine speeds. SFC was decreased by 5.3% and 2.9% at low and high engine speeds, respectively. Also, hydrocarbons and CO emissions were decreased at high engine speeds by retarding the IVC.

## 2.6 Sudhakar (2001)

A paper by Sudhakar (2001) investigates the failure of an automotive valve spring. The spring failed prematurely during service. In order to determine the reason for the fracture, the fracture surface and the material in proximity to the fracture surface were examined in a Scanning Electron Microscope (SEM). Optical microscopy was also performed in order to evaluate the basic microstructure of the material. The paper concludes that the failure occurred due to the presence of non-metallic inclusions near the surface of the spring material. This is not expected to be the problem in the case of the valve springs of the 2018 Honda CRF 250R engine, but can still be relevant to evaluate.

## 2.7 Bortoli et al. (2010)

The purpose of the paper written by de Bortoli et al. (2010) is to evaluate the helical suspension spring system of a hermetic compressor. They are looking into the aspects of noise and vibration and how these factors effect the springs. Also during the start/stop motion of the engine it is important that the crankcase does not hit against the housing, and therefore the stiffness of the spring is vital in order to have a good balance between vibration and displacement. Finally, this study looks into how the service life of the springs are affected by the stiffness of the spring. This is done based on numerical, and experimental analyses, to evaluate the fatigue life of the spring suspension system.

## 2.8 B.Pyttela et al. (2014)

In a study conducted by B.Pyttela et al. (2014), long-term fatigue tests on shot peened helical compression springs were conducted by a special testing machine running cycles of 40 Hz. The springs in the studies were made of three different spring materials; oil hardened and tempered SiCr- and SiCrV-alloyed valve spring steel and stainless steel.

Springs with two different wire diameters, d = 3.0 mm and d = 1.6 mm, were tested at different stress levels. Based on fatigue investigations of springs with d = 3.0 mm up to a number of $N = 10^9$ cycles, an analysis was done. Afterwards the test was continued to $N = 1.5 \times 10^9$ cycles and the results were compared. The influence of different shot peening conditions were investigated for the springs with the smallest diameter. Springs that fractured during testing were examined under optical microscope, SEM, and by means of metallographic microsections in order to analyse the fracture behaviour and the failure mechanisms.

The study concludes that fracture can occur at any position in the coil. Also it is established that springs are very sensitive to inclusions. For this reason, their size and number have to be minimised in the process of material making, wire drawing and finally construction of the springs.

## 2.9 C.Berger and B.Kaiser (2006)

A study conducted by C.Berger and B.Kaiser (2006) presents the first results of very high cycle fatigue tests on helical compression springs. The springs in this study are manufactured of Si–Cr-V-alloyed valve spring wire, which is shot-peened and preset. This is similar to the materials and production processes assumed to be utilised for the 2018 Honda CRF 250R valve springs.

The fatigue limits of these springs are evaluated from running test of $N = 10^7$ cycles, and compared with the fatigue strength when the fatigue tests are continued up to $N = 10^8$ cycles and beyond. The fatigue limits are calculated by statistical evaluation according to the arcsin $\sqrt{p}$ -method, and is found to be 1038, 1006 and 972 MPa for a survival probability of 10%, 50% and 90% respectively, for $N = 10^7$ cycles. These values are given as the "corrected stroke stress". It is established that an increase of the cycles from $N = 10^7$ to approximately $N = 10^8$ cycles results in a nearly 10% reduction of the fatigue limit for 90% survival probability, while an increase from $N = 10^7$ cycles to $N = 1.2 \times 10^9$ cycles reduces the fatigue limit for 90% survival probability by approximately 25%.

Finally, the study investigates the fractured springs using a SEM. From this analysis it is concluded that nucleations of fracture tend to occur below the surface if the fracture happens after more than $N = 10^7$ cycles. It also shows that the typical fracture initiation sites is without non-metallic inclusions.

Chapter 3

# Basic Theory

Some parts of this chapter is taken from the semester project ”High performance cam profile design and optimization” written in the fall of 2018 by the signatory. As the main objective of the task remains the same, most of the theory is considered relevant for this master thesis. Some complementary theory is also added.

## 3.1 Cylinder Head, Valve and Camshaft Assembly

The four valve springs in the 2018 Honda CRF250R engine can be seen in the centre of Figure 3.1. They are located between the engine head and the valve retainer. The end of the spring resting against the engine head is stationary, while the opposite end, at the spring retainer, moves along with the valve when the valve head is pushed. This is what makes the spring compress.

The assembly of the valve and springs can be seen in Figure 3.2. Even though the intake and exhaust valves are slightly different when it comes to the length, stiffness and movement during operation, the assembly is the same.

Because of the importance of the valve closing properly, the valve spring is pre-tensioned during assembly so that there are always a closing force acting on the valve.

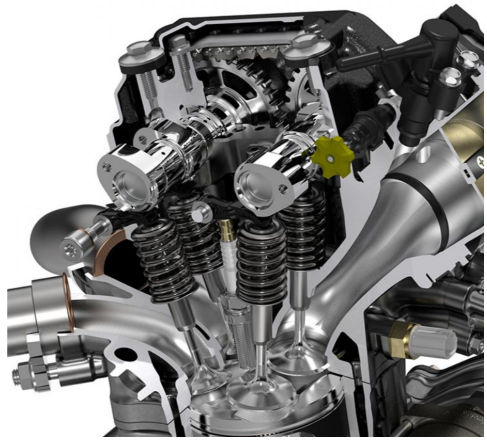

**Figure 3.1:** Honda CRF250R 2018 engine.[Honda Motor Company (2018)]

## 3.2 Camshaft Profile

In the Honda engine the valves are operated by overhead rockers which are constantly sliding against the camshaft, and therefore following the cam profile. It is important that the design of the camshaft profile is constructed in such a way that the valve never jumps i.e. it prevents the follower mechanism from losing contact with the camshaft during operation. This will lead to unpredictable loading situations in the valve assembly and give an unwanted valve operation. However, when the valve is closed, a valve clearance of the magnitude of 0.1 mm is desired in order for the valves to seat properly, making sure the intake/exhaust remains sealed when closed. The translation from the circular movement of the camshaft, to the vertical, linear movement of the valve, is generated by the camshaft lobes. Thus the exact profile of these lobes is crucial to how the valve is operated. The lobe profile together with the rocker arm determines the lift curve, velocity, acceleration and jerk of the valve movement. Finally, the shape of the lobe determines the valve timing.

### 3.2.1 Valve Timing

Since the crankshaft is rotated twice for each power stroke, and the intake and the exhaust valves only should be opened once during the full cycle, the camshaft is connected to the crankshaft with a gear ratio of 2:1. The timing of the valves is measured from 0.050 inch of lobe lift (1.27 mm). Valve timing is crucial for the characteristics of the engine, and it effects the power, emission and torque of the engine. The valve opening and closing is usually given in terms of degrees of crankshaft rotation.

Figure 3.3 shows a typical valve timing diagram. As seen in the figure the Inlet valve

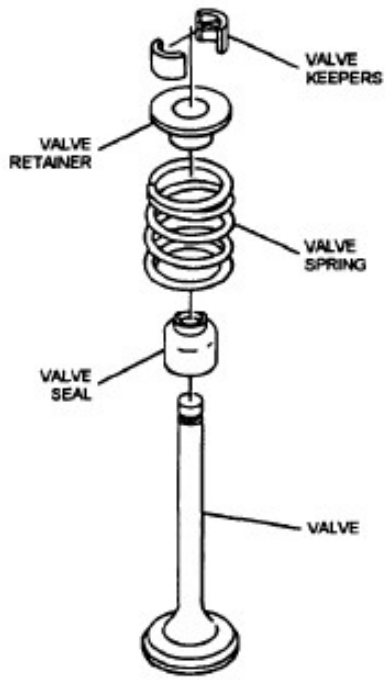


**Figure 3.2:** Valve spring assembly.[It Still Runs (2018)]

Opens (IO) before the Top Dead Centre (TDC) and the Inlet valve Closes (IC) after the Bottom Dead Centre (BDC). On the other hand the Exhaust valve Opens (EO) before the BDC and the Exhaust valve Closes (EC) after the TDC. This means that there will be some overlap where both the intake and exhaust valves are open at the same time between the exhaust and intake stroke (the black part of the figure). The reason for this can be explained by looking at what the engine is optimised to do.

**Duration**

When the engine is running at a high RPM, a longer duration of the opening of the inlet valve is desired if the goal is to have a powerful engine. This is because it allows for more air to enter the combustion chamber [Mechadyne International Limited (2006)]. The intake valve duration can, and should, actually exceed the 180 degree intake stroke for a high RPM engine in order to maximise the power output. The reason why this is preferred, is due to the inertia of the air entering the combustion chamber. Therefore, it is desirable to keep the inlet valve open for the first part of the compression stroke in order to let the already moving air enter, finally providing an engine with high power at the given RPM. The drawback with too long duration is that the torque at low RPM will be low, making it necessary to ”rev” the engine when releasing the clutch in order to not choke the engine. This is why an inlet duration of 180 degrees is preferable at low RPM, at least if the valves

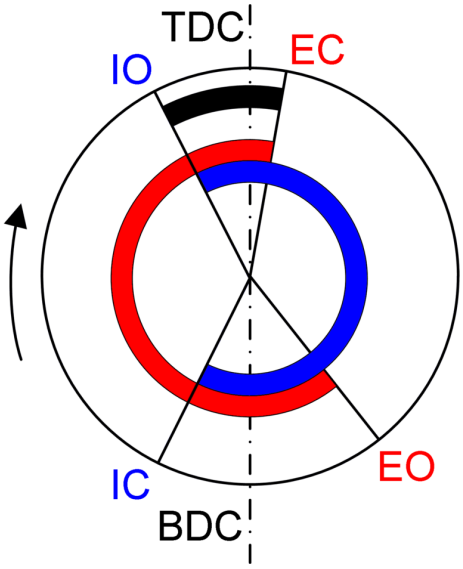


**Figure 3.3:** Valve timing diagram for a 4-stroke engine. [Rios (2018)]

were to open and close instantly. A longer duration than this will allow for air to escape at low RPM, something that is not desirable when the goal is to produce torque.

**Overlap**

In order to increase the duration, the IO is typically before the TDC, giving an overlap where both the intake valve and exhaust valve are open at the same time. The magnitude of this overlap vary a lot, but all racing engines will have a significant amount of overlap. This is done so that the moving flow of exhaust gases can pull the new charge of air and fuel mixture into the cylinder, and therefore replace the residue exhaust gas in the combustion chamber at TDC, allowing for a greater amount of intake charge in the cylinder than what could have been achieved by the swept piston alone. It is important that the amount of overlap is well timed. An excessive overlap will cause some of the new charge to flow straight through the cylinder together with the exhaust gases, leading to poor fuel efficiency of the engine. Unfortunately, the ideal overlap is very dependent on engine speed, and an overlap optimised for high RPM performance will give poor fuel economy and release more uncombustioned fuel at lower speeds. High amount of overlap can also lead to Exhaust Gas Recirculation (EGR), something that can be beneficial in terms of emission because a more complete combustion is achieved [Mechadyne International Limited (2006)]. On the other hand, this reduces the torque if it happens at full load and provides an unstable combustion at low loads.

**Intake valve closing/opening**

The IO is one of the two parameters effecting the overlap. By opening the intake valve

before the TDC, the new air and fuel mixture is allowed to fill the small volume of the combustion chamber when the piston is at the TDC. This makes it possible to get a larger amount of air and fuel mixture to enter during the intake stroke. If the IO is shifted even earlier, the EGR will be increased and hence a better efficiency at partial load can be achieved at the cost of reduced torque at maximum load.

Typically the IC is set to be sometime after the BDC. The optimal IC for maximum torque is the timing where the greatest amount of fresh air and fuel mixture is trapped in the cylinder. This instance is highly dependent on the engine speed. For an engine running at a high RPM the IC should be moved further after BDC, as this will allow for more of the already moving air and fuel to enter. At low engine speeds however, a late IC will result in some of the mixture flowing back into the intake manifold and therefore reducing the torque [ÇINAR and AKGÜN (2007)].

**Exhaust valve closing/opening**
The EO is typically sometime before the BDC. By opening the exhaust valves early, some of the pressure from the combustion is allowed to escape through the exhaust system, losing the potential work this gas could have done by acting on the piston. On the other hand, by doing this, the pressure in the cylinder will be lower when the piston starts to rise, resulting in a smaller amount of work necessary in order for the piston to expel the exhaust gases [Mechadyne International Limited (2006)]. To summarise, the EO is a trade-off between the work lost by letting the exhaust gases escape during combustion, and the extra work required in order to raise the piston when the pressure in the cylinder is above the exhaust back-pressure. In order to determine the optimal EO, it is relevant to look at the valve speed and acceleration. In a conventional engine, the valves will lift from their seats slowly, requiring an earlier EO. The optimal timing is also dependent on the engine speed. Generally an early EO is desirable for high speed engines operating at max load. At lower speeds and part load, an EO closer to BDC is favourable as the exhaust back-pressure is lower and the exhaust gases have more time to escape the cylinder.

The EC is typically sometime after the TDC. The EC is the second factor defining the valve overlap, and it has a large impact on the amount of exhaust gas that is left in the cylinder before the intake stroke. When the engine is operating at max load and high speed, it is desirable to minimise the amount of residue exhaust gases, as this will result in a smaller amount of fresh air and fuel mixture entering the cylinder. Therefore, an EC shortly after the TDC is preferable for these conditions. On the other hand, if the engine is operating on partial load, a later EC might be preferable as this will increase the amount of EGR, something that will give a better, more complete combustion and therefore reduced emissions and fuel consumption. However, there is a limit to how much EGR that is possible while still maintaining a stable combustion.

## 3.3 Engine Cycles and Valve Operation

The Honda CRF250R 2018 is a four stroke engine. The four strokes are shown in Figure 3.4 and can be roughly separated as follows:

- Intake:
  During the intake stroke, the air and fuel mixture is entering through the intake valve due to the vacuum generated by the downward motion of the piston. The intake stroke lasts from the TDC to the BDC.

- Compression:
  During the compression stroke, all of the valves are closed while the piston moves up from the BDC to the TDC, and the fuel and air mixture is compressed.

- Power:
  The valves stays shut during this stage. The power stroke starts when the spark ignites the air and fuel mixture, and the piston is at the TDC. Power is generated as the piston is pushed by the explosion to the BDC.

- Exhaust:
  The exhaust valve is opened, and the piston moves from the BDC to the TDC, while it forces the exhaust out through the exhaust valve.

As described in the section 3.2.1, the valve operations does not perfectly follow the four strokes. Typically, it will start and end sometime between the strokes, depending on the type of engine and its characteristics.

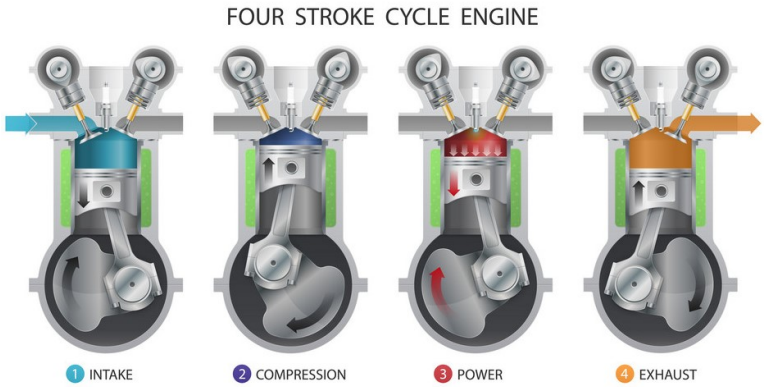


**Figure 3.4:** Four stroke engine cycles.[Vectorstock (2018)]

## 3.4 Valve Springs

The valve springs are a central part of the valve train, whose main functions are to lift the mass of each valve during the closing operation, and to produce just the right amount of friction between the cam follower and the camshaft. This is important, as these parts should be in contact during the valve operations, so that the cam follower accurately follows the cam profile.

Figure 3.5 shows a simplified model of the parts interacting with the valve springs in the valve train of the engine.

**Figure 3.5:** Simplified model of the relevant parts of the valve train.

### 3.4.1 Material and Production

High performance valve springs are manufactured from special, high-tensile-strength alloys of very high purity, and later subjected to various surface treatments in order to have the desired properties.

The high performance valve springs of the 2018 Honda CRF 250R are assumed to be of Si–Cr-V-alloyed valve spring wire, quenched and tempered according to the A877 standard. The springs are assumed to be shot-peened, a cold working process used to produce a residual stress layer in order to make the springs resistant to fatigue failure. The chemical composition of the springs is shown in Table 3.1. The density of the material is estimated to $\rho = 7.73 g/m^3$ by using the average of the chemical compositions described in the table.

| C | Si | Mn | P (max) | S (max) | Cu (max) | Cr | V |
|---|---|---|---|---|---|---|---|
| 0.50–0.60 | 1.20–1.60 | 0.50–0.90 | 0.025 | 0.020 | 0.006 | 0.50–0.80 | 0.15–0.25 |

**Table 3.1:** Chemical composition of Si–Cr-V-alloyed valve spring. [Compass ASTM (2019)]

The spring wire used for the valve springs in question is elliptical, therefore an average diameter of 3.4 mm is assumed. By interpolation from Table 3.2, the Ultimate Tensile Strength (UTS) is therefore set to $\sigma_{UTS} = 2116$, the average between the max and min for for the interpolated value.

| Diameter [mm] | MPa, min | MPa, max | Min % R.A |
|---|---|---|---|
| 3.0 | 2070 | 2200 | 40 |
| 3.75 | 2030 | 2170 | 35 |

**Table 3.2:** Mechanical properties of Si–Cr-V-alloyed valve spring when Quenched and Tempered. Ultimate tensile strength, max and min, and reduction of area (% R.A.). [Compass ASTM (2019)]

### 3.4.2 Spring Theory

The maximum shear stress in a helical spring is given by equation 3.1. W is the axial force acting upon the spring.

$$\tau_{max} = K_w \left( \frac{8WD}{\pi d^2} \right) \tag{3.1}$$

Due to the curvature in the spring, the stress concentration is considerably higher in the inner part of the coils than on the outer parts [Jindal (2010)]. For this reason, Wahl's factor $K_w$ is introduced in order to take the curvature into account. It is given by the equation:

$$K_w = \frac{4C - 1}{4C - 4} + \frac{0.615}{C} \tag{3.2}$$

where the spring index C is given by the relation, C=D/d. Figure 3.6 shows the different spring parameters of a helical spring.

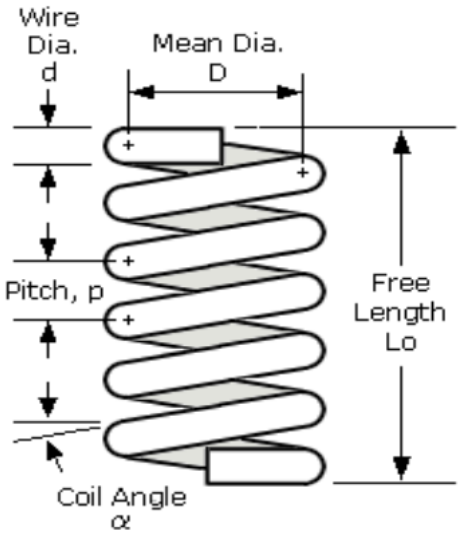


**Figure 3.6:** Spring parameters.[Engineering (2019)]

### 3.4.3 Problems Related to Valve Springs

There exists a number of different problems with the valve train that are related to the valve springs. Two of the most common ones are:

#### Valve Float

Valve float is the term for a condition typically occurring in engines running at high RPM when the cam follower do not follow the closure phase of the cam lobe. This is a result of the cam profile being too aggressive compared to the closing force produced by the valve springs, and the mass of the valve assembly, leading to a floating phase where the cam follower lose contact with the cam. The result of this is usually reduced engine efficiency and performance. There is also a high risk of damaging the valve springs [Vizard (1991)].

#### Valve Bounce

When the valves fail to stay seated, and instead bounce off the seat just after closing, it is called valve bounce. This condition can be related to valve float, and it is a result of the closing velocity of the valve toward the seat being too high, or the spring force being too low. Effects like resonance in the valve spring, leading to a reduced closing force, can also contribute to this condition [Vizard (1991)].

## 3.5 Young's Modulus Dependency on Temperature

The Young's Modulus is dependent on the temperature of the material. As the temperature increases, the stiffness of the material decreases. This should be taken into account as the temperatures in the engine can reach such elevated levels that it has a significant impact on the stiffness of the valve springs. Wang et al. (2013) develop a relationship between temperature and Young's Modulus for HSS Q460 steel. It is given by the following equation:

$$\frac{E_T}{E} = 1.02 - 0.035e^{\frac{T}{280}} \qquad 20°C \leq T \leq 800°C \tag{3.3}$$

Even though this equation is based on empirical data obtained from samples made of HSS Q460 steel, it gives a good approximation for other types of steel with similar properties. As spring steel typically is some form of high strength steel alloy, equation 3.3 is used to determine the Young's Modulus for the material of the spring at different service temperatures.

## 3.6 Natural Frequencies

The natural frequencies of a structure are the frequencies at which the structure naturally tends to vibrate if it is subjected to a disturbance [Henderson (2018a)]. This is also called the eigenfreqencies of the structure. Multiple factors influence the frequency at which an object will vibrate. The common denominator for all of these are that they all either affect the wavelength, or the speed of the vibrations, of the object. This can be seen from the following equation for frequency:

$$frequency = speed/wavelength \tag{3.4}$$

Some of the most important factors that influence the natural frequency is the stiffness and the mass of the structure.

### 3.6.1 Resonance

Resonance is a phenomenon in which a dynamic force drives a structure to vibrate at its natural frequency [Henderson (2018b)]. When a structure is subjected to an oscillation that matches the structures natural frequency, the amplitude of the oscillations will increase even though the force that acts upon the system stays constant. This makes it possible for a small force to generate large vibrations, and even catastrophic failures of components, even though the driving force is well bellow the critical limits for the material of the component.

### 3.6.2 Modes

The mode of a structure is defined as follows: ”The deformed shape of the structure at a specific natural frequency of vibration is termed its normal mode of vibration”, [Siemens AG (2014a)]. The normal mode of vibration can also be called mode shape, characteristic shape, and fundamental shape. Every natural frequency of an object has an associated mode shape. This means that the structure will deform as a result of the vibration, but in different ways depending on the frequency of the driving force.

As described earlier the natural frequency is dependent on the structural properties of the object. This means that if the properties of the object change, the natural frequencies will change as well. The mode shapes on the other hand, might stay the same.

The natural frequency is also dependent on the boundary conditions of the given object. As a result, a change in the boundary conditions will lead to a change in the natural frequency. Additionally, the mode shape will change.

## 3.7 Rayleigh Damping

Proportional damping, or Rayleigh damping, use a linear combination of the mass and stiffness matrices in order to form the stiffness matrix C,

$$C = \alpha_1 M + \alpha_2 K \tag{3.5}$$

where $\alpha_1$ and $\alpha_2$, denotes the mass proportional and stiffness proportional damping respectively.

The mass proportional damping forces are generated from the absolute velocities of the nodes in the model. This is comparable to the the damping generated by a model moving through a fluid, where the model is experiencing damping generated from the fluid from any moving points of the model. Reasonable mass proportional damping does not significantly reduce the stability limit. However, it might introduce unwanted drag effects at large displacements and speeds, and must therefore be applied with care in these scenarios [RØLVÅG (2018)]. If the damping ratios $\lambda_1$ and $\lambda_2$ for two damping modes are selected, the mass proportional damping constant can be calculated using the following equation:

$$\alpha_1 = \frac{2\omega_1\omega_2}{\omega_2^2 - \omega_1^2}(\lambda_1\omega_2 - \lambda_2\omega_1) \tag{3.6}$$

The stiffness proportional dampening is generated from a ” damping stress” proportional to the total strain rate. Stiffness damping can be utilised for any non-linear analysis. However, it can significantly reduce the stability limit, and should therefore be used with cau-

tion [Ding and Ye (2006)]. The stiffness proportional damping constant can thus be calculated using the following equation:

$$\alpha_2 = \frac{2(\omega_2\lambda_2 - \omega_1\lambda_1)}{(\omega_2^2 - \omega_1^2)} \tag{3.7}$$

## 3.8 Fatigue

Fatigue describes the phenomenon where structures fail due to accumulated damage from the application of cyclic loads, where each load may be imposing stress levels well below the yield stress of the material.

Empirical methods for quantifying the fatigue process in order to be able to design against it have been developed. The most important concept is the S-N diagram, also known as the Wöhler curve. This is established by applying a constant cyclic stress amplitude to a specimen and count the number of loading cycles, N, until failure for each stress level. For some materials, mainly ferrous alloys, the S-N curve flattens out for some given stress level, called the endurance limit $\sigma_e$. Because millions of cycles might be required to cause failure at lower loading levels, the x-axis of the diagram is usually plotted logarithmically. [Roylance (2001)]

In some cases, the actual loading scenario does not involve a fully reversed stress cycle. Therefore, fatigue tests can be performed with a mean stress, $\sigma_m$, on which a sinusoidal cycle is superimposed, as shown in Figure 3.7. This cycle is fully defined by specifying the alternating stress, $\sigma_{alt}$, and the stress ratio given by $R = \sigma_{min}/\sigma_{max}$.

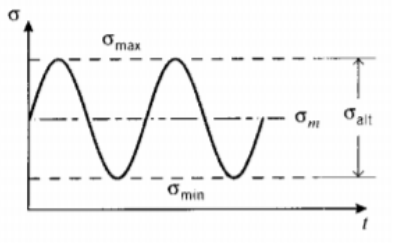


**Figure 3.7:** Illustration of simultaneous mean an cyclic loading. Roylance (2001)

Because it is both time consuming and costly to determine S-N curves for every combination of mean and alternating stress, the Goodman diagram shown in Figure 3.8 is used to approximate the endurance limit for different loading scenarios. This diagram is constructed by drawing the so called Goodman line from the endurance limit, $\sigma_e$, to the UTS of the material, $\sigma_f$. For any combination of an alternating stress, $\sigma_{alt}$, and mean stress, $\sigma_m$, within the area under the curve, the material should not fail. [Roylance (2001)]

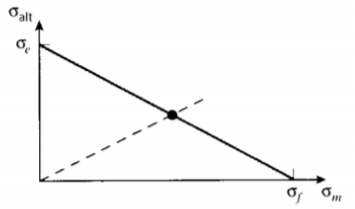


**Figure 3.8:** The Goodman diagram.[Roylance (2001)]

### 3.8.1 Designing the S-N Curve

According to the standard DNV GL, RP-C203, the basic design of an S-N curve is given by the relation [DNV GL AS (2016)]:

$$logN = log\bar{a} - mlog\Delta\sigma \tag{3.8}$$

with the following parameters:

- N = predicted number of cycles to failure for stress range $\Delta\sigma$
- $\Delta\sigma$ = stress range with unit MPa
- m = negative inverse slope of S-N curve
- $log\bar{a}$ = intercept of log N-axis by S-N curve

In FEDEM, the S-N curve is defined by lines described by the pairs 'log(an)' and 'mn', as defined by the DNV GL standard. Each of the pairs are handled consecutively. The line described by 'log(an)' and 'mn' ends with the crossing of the line defined by the 'log(an+1)' and 'mn+1' pair, until all pairs are read [Fedem Technology AS (2016b)].

## 3.9 General Introduction to FEA

Finite Element Analysis (FEA) is the modeling and analysis of structures in a virtual environment. This makes it possible to detect and solve a wide range of problems. FEA is the application of Finite Element Method (FEM), and it is used to mathematically model and numerically solve complex problems [Siemens AG (2019)].

The Finite Element (FE) model is constructed on the basis of a system of points called nodes. The nodes are forming the geometry of the part of interest. The FE mesh is formed

by the finite elements. This contains the material and structural properties of the model, and defines how each of the elements, and therefore the part itself, will react to given conditions and loading scenarios. Because some areas of a part can be of greater interest than others, and some regions might experience higher stress changes, the density of the FE mesh can be varied in order to best capture the actual situation [Siemens AG (2019)]. Below follows an overview of some of the elements available for FEA, all of which are used for this master thesis.

### 3.9.1 CTETRA(10)

The CTETRA(10) element is a three-dimensional element, a solid element with four sides (tetrahedral) and 10 grid points, also known as nodes. The element is shown in Figure 3.9. Because this is a solid element, it only has translational Degree of freedom (DOF), and therefore no rotational DOF are used to define the element. Due to the geometry of this element, it has a distinct advantage over for example CHEXA elements when the CAD model has sharp corners, as CTETRA elements can be better shaped than CHEXA elements [Siemens AG (2014b)].

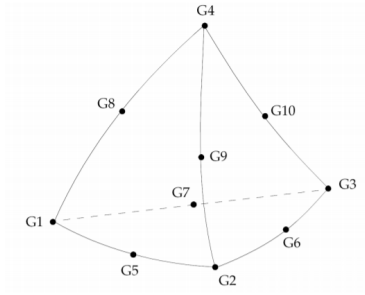


**Figure 3.9:** The CTETRA(10) 10 node element. [Siemens AG (2014b)]

### 3.9.2 CHEXA(8)

The CHEXA(8) element is also a solid element, but with six sides (brick) and 8 grid points, nodes. The CHEXA(20) elements is shown in Figure 3.10. It is identical to the CHEXA(8), except that this element, in contrast to CHEXA(8), includes midside nodes. This element also only have translational DOF, and no rotational DOF are therefore used to define the element. While the CHEXA element is recommended for general use, the CHEXA's accuracy degrades when the element is skewed [Siemens AG (2014b)].

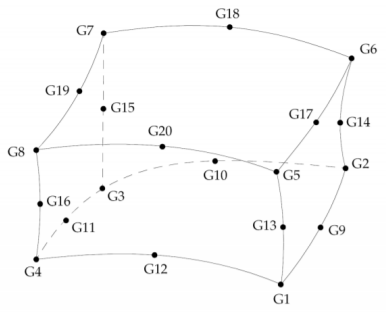


**Figure 3.10:** The CHEXA(20) 20 node element. [Siemens AG (2014b)]

### 3.9.3 CQUAD4

The CQUAD4 element is a two-dimensional element, a surface element with four sides (quadrilateral) connecting the four grid points. The element and its coordinate system is shown in Figure 3.11. It is used to represent a structure whose thickness is small compared to its other dimensions. Because this is a plate element, each node only have a stiffness in five of the possible DOF's. This is because there is no stiffness associated with the rotation about the normal vector of the plate [Siemens AG (2014b)].

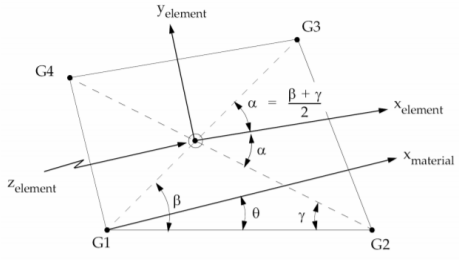


**Figure 3.11:** The CQUAD4 4 node element with element coordinate system. [Siemens AG (2014b)]

### 3.9.4 Rigid Body Element, Form 2

The Rigid Body Element, Form 2 (RBE2) element defines a rigid body by selecting an independent node, a master node, and multiple dependent nodes, slave nodes. The RBE2 element use constraint equations to couple the motion of the slave node DOF to the motion of the master node DOF. Because RBE2 elements do not contribute directly to the stiffness matrix of the structure, ill-conditioning of the stiffness matrix is avoided, even though the stiffness of the RBE2 in itself is infinite [Siemens AG (2014b)].

## 3.10 General Introduction to FEDEM

The FEDEM software provides a platform for virtual testing of complex mechanical assemblies. FEDEM is an acronym for "Finite Element Dynamics in Elastic Mechanisms", [Fedem Technology AS (2016b)]. It includes features to create, solve and post-process a model in a 3D graphical environment. It also provides postprocessing capabilities, stress analysis, eigenmode solutions, strain gauge solutions and fatigue analysis for selected time steps.

### 3.10.1 Dynamic Analysis

The dynamic analysis in FEDEM provides the time dependent displacements, velocities, accelerations, and derived secondary quantities in the mechanical system driven by external forces and/or prescribed displacements, velocities and accelerations. Dynamic analyses are generally more expensive than static analyses in terms of computational power, because the solution involves repeated computations of the same form, whereas static analysis requires only a single computation. The introduction of Component Mode Synthesis (CMS) model reduction and super element techniques, as utilised by the FEDEM software, reduces the cost of dynamic computations, as the CMS reduction technique decreases the number of DOFs used [Fedem Technology AS (2016a)].

### 3.10.2 Modal Analysis

The dynamic analysis makes it possible to calculate the eigenmodes, the eigenfrequencies of the system, at different mechanism positions during the simulation time. By running a mode shape recovery analysis, the corresponding modes shapes can be extracted for the specified simulation steps.

### 3.10.3 Fatigue Analysis

FEDEM utilises the reading from a virtual strain gauge as the input for the fatigue analysis. The data is simplified using a threshold value in order to filter out small oscillations that are not relevant for the result, called peak valley extraction. Rainflow counting is performed so that the data is represented as a set of stress/strain reversals [Fedem Technology AS (2016a)]. Finally, a damage and life calculation is performed based on this data. Accumulated damage is computed by summing up all the individual setts of stress ranges, $\bar{\sigma}_i$, i =1...k, with the corresponding number of cycles before failure, $N_i$, for the given stress level and the S-N curve of the material. This is expressed as:

$$C = \sum_{i=1}^{k} \frac{1}{N_i} \tag{3.9}$$

where failure occurs when $C >= 1.0$. The estimated life span of the part is finally given as the relation between the simulation time, $T_s$, and the estimated damage per simulation:

$$Life = \frac{T_s}{C} \tag{3.10}$$

## 3.11 General Introduction to Siemens NX

NX is an advanced high-end CAD, Computer Aided Manufacturing (CAM) and Computer Aided Engineering (CAE) software, which has been owned since 2007 by Siemens AG. It is used in all of the steps of the product development, from product design and engineering analysis, to manufacturing and planning of the parts.

### 3.11.1 NX Nastran

NX Nastran is a FEM solver integrated in Siemens NX. It includes solutions for linear and nonlinear structural analysis, dynamic response, acoustics, rotor dynamics, aeroelasticity, thermal analysis, and optimisation.

**SOL 103: Real Eigenvalue Analysis** NX Nastran includes multiple solvers for extracting real eigenvalues. For this paper, the Real Eigenvalue Analysis (SOL 103) is used for the simple eigenvalue analysis of the spring itself. NX Nastran includes seven different methods of real eigenvalue extraction. These methods are numerical approaches to solving for natural frequencies and mode shapes. The recommended real eigenvalue extraction method in NX Nastran is the Lanczos method. The Lanczos method combines the best characteristics of both the tracking and transformation methods. For most models the Lanczos method is therefore the best method to use. It is also usually one of the faster methods when high number of eigenmodes are necessary and there are many degrees of freedom [Siemens AG (2014a)]. The general expression used to compute the eigenfrequencies for the undamped system is the matrix relation expressed in Equation 3.11,

$$(-\omega^{\mathbf{2}}\mathbf{M} + \mathbf{K})\boldsymbol{\phi} = \mathbf{0} \tag{3.11}$$

where $\omega$ is an angular velocity, $\mathbf{M}$ is the mass matrix, $\mathbf{K}$ the stiffness matrix and $\boldsymbol{\phi}$ is the eigenvector of the system. Equation 3.11 can be rewritten as Equation 3.12, which only

has a nonzero solution for $\boldsymbol{\phi}$ if det($\mathbf{A}$) = 0. This leads to the stiffness matrix' inability to be inverted, and hence an unstable structure, [Gavin (2012)].

$$\mathbf{A}\boldsymbol{\phi} = \mathbf{0} \tag{3.12}$$

**SOL 601: Advanced nonlinear static** The SOL 601 is a solver that makes it possible to analyse models with nonlinearity from contacting parts, material nonlinearities and/or geometric nonlinearities (that is, large deformations) [Siemens AG (2011)]. The advanced nonlinear solver is an integration of the ADINA solver into NX Nastran.

For certain analysis purposes, geometric nonlinear effects needs to be simulated. This is the case when stiffness properties or loads change significantly as the result of deformation. In order to have a realistic evaluation of the valve spring during compression, large deformations has to be taken into account. This solver also includes advanced contact capabilities that makes it possible to simulate surface contact using either shell or solid elements. The solver also determines the extent of surface contact and load transfer across the contacting surfaces as part of the solution.

Chapter 4

# Experiment

The first part of this chapter describes how the exhaust valve spring was modelled for the semester project ”High performance cam profile design and optimization” written by the signatory. As this spring is still the component to be evaluated in this masters thesis, this part of the chapter is also included here.

## 4.1 Valve Spring CAD Model

The helical valve spring of the Honda CRF 250R is modelled using Siemens NX. In order to make a precise 3D representation of the spring, the original spring is measured using a caliper. The spring has an overlap of 4 mm between the upper and the lower coil. The gap between each of the coils is measured in order to determine the pitch of the spring. Since the spring has a variable pitch, it was measured at four points for each rotation as seen in Table 4.1

| Coil | Angles | 0 | 90 | 180 | 270 |
|---|---|---|---|---|---|
| 1 | | 0 | 0.25 | 0.80 | 1.00 |
| 2 | | 1.00 | 1.25 | 2.00 | 2.60 |
| 3 | | 3.40 | 3.70 | 3.80 | 3.80 |
| 4 | | 3.80 | 3.80 | 3.80 | 3.80 |
| 5 | | 3.80 | 3.80 | 3.80 | 3.80 |
| 6 | | 3.80 | 3.20 | 2.20 | 1.20 |
| 7 | | 0.10 | | | |

**Table 4.1:** Spacing between coils measured at four points per turn. [mm]

The pitch can now be calculated for each part of the spring by using the spacing and adding the vertical diameter of the spring. The pitch between each of the measuring points was assumed to be linear. Because parts of the spring has a constant pitch, the coil was finally modelled as 9 separate coils rotating between 0.5 and 2.5 round each in order to make the full 7 coils of the spring.

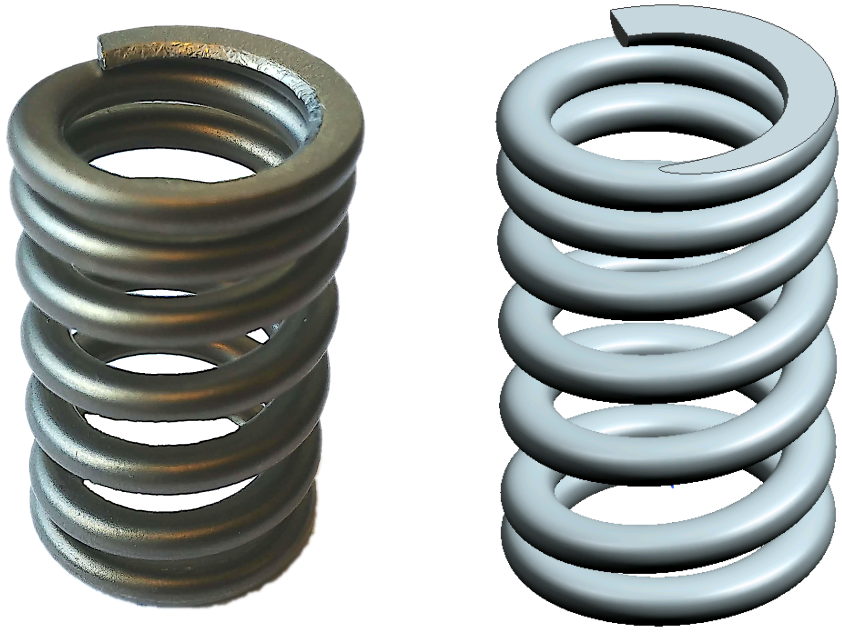

**(a)** Physical spring

**(b)** CAD model

**Figure 4.1:** Valve spring.

The path for the coils were represented using the helix function in Siemens NX. In order to model the spring, the swept function was used with the helix as the path and swept over the cross section. Finally, the extrude function with the subtract option was used in order to flatten each of the ends of the spring. The CAD model and the physical spring is shown in Figure 4.1.

### 4.1.1 Cross Section

The cross section of the spring is only measured at two different points, vertically and horizontally. As the spring does not have a perfect elliptic shape, it is possible to adapt the cross sectional area in order to have a satisfying spring stiffness. This was done in iterations during the semester project. By defining the four measured points, namely the

large diameter of 3.8 mm and the small diameter of 3 mm, and modifying the curve between these points using the studio spline function, a new slightly larger cross section is obtained. The comparison of the perfect elliptic and the modified cross section can be seen in Figure 4.2.

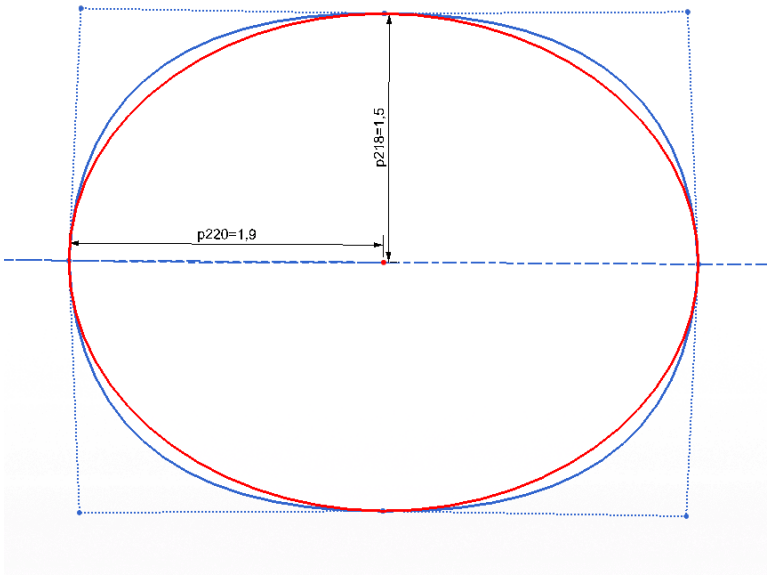


**Figure 4.2:** Perfect elliptic cross section in red. Modified cross section in blue.

### 4.1.2 Mesh

The spring was partitioned so that it could be meshed as three different parts. This is done so that the ends of the spring can be meshed in a finer mesh, in order to capture the details of the spring. The meshing was done in iterations, controlling the quality of the mesh each time. Finally, the two ends were meshed with an element size of 0.8 and no curvature based size allowance. The middle part of the spring was meshed with an element size of 1 mm and a surface curvature based size variation of 26%. A 3D thetra mesh with CTETRA(10) elements was used for all of the partitions. The element quality was controlled using the built in function in NX, yielding 0 failed elements and 587 warning elements out of the total 48132 elements. Finally, a RBE2 element was added to the top face of the spring. The meshed spring can be seen in Figure 4.3. The spring was assigned the following material properties, a Young's Modulus (E) of 206.94 GPa and a Poisson's Ratio ($\nu$) of 0.288 at 20 °C and a mass density of 7732 $kg/m^3$.

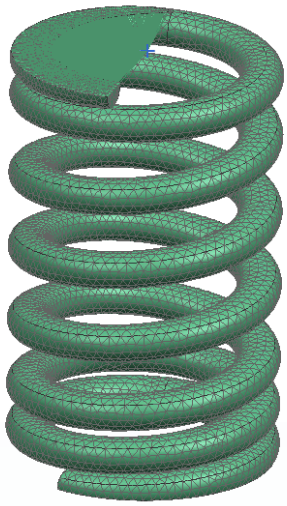

**Figure 4.3:** Meshed spring.

### 4.1.3 Verification

#### Total length

In order to verify the accuracy of the CAD model, the total length of the physical spring was compared with the one of the CAD model. The length of the physical spring was measured to 36.90 mm while the CAD model has an overall length of 37.15 mm, resulting in a deviation of 0.25 mm, or 0.68 %, over the total length.

This error might derive from small errors in each of the measurements of the individual coils, and consequently sum up to a greater error in total. In Figure 4.4 the helix is displayed with measurements at given points. These measurements correspond well with the ones from Table 4.1.

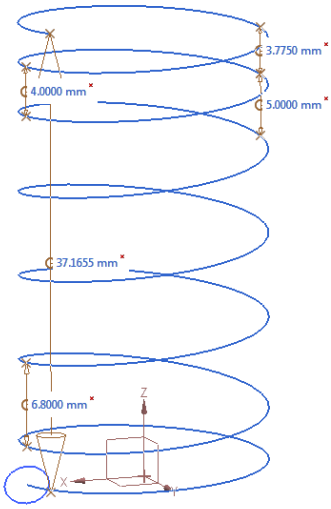


**Figure 4.4:** Helix with measurements.

### Total Mass

The mass of the modelled spring can now be verified by comparing it to the mass of the physical spring, which is measured using a letter scale. The modelled spring is measured using the ”measure body” function in NX. This function determines the mass by using the selected material properties. As the exact material properties are unknown, the density calculated in section 3.4.1 are used. This gives a mass density of 7733 $kg/m^3$. Steel typically has a density of 7700-8000 $kg/m^3$, depending on the alloy.

The modelled spring has a volume of 4035 $mm^3$, and a mass of 31.20 g. Both of the measurements conducted in NX has a negligible error estimate of the magnitude 0.002 g.

The physical springs are measured to 30.84 g with an accuracy of 0.01 g. This corresponds to a total error of the magnitude 0.4 g for the modelled spring compared with the physical spring. This can be a result of the cross section of the modelled spring having a marginally larger cross-sectional area than the physical spring, or the fact that the total length of the modelled spring is slightly larger then the physical spring. Both these factors will contribute to a greater mass of the modelled spring.

### Spring Stiffness

For the results from the eigenvalue analysis to be accurate, it is important that the stiffness of the physical spring is well represented in the model. In order to verify the accuracy of the CAD model, a compression analysis was executed on the modelled spring, and compared with the force/displacement diagram for the physical spring seen in Figure 4.6.

In order for the loading scenario to be realistic, the whole top plane of the spring has to be compressed. Therefore, a steel plate with a thickness of 5mm was introduced. This plate was constrained, so that only movement in the z-direction was allowed in order to compress the spring. For interaction between the spring and the plate, surface-to-surface gluing was selected as simulation object type. For the self contact between the individual spring coils, surface-to-surface contact with a static friction of 0.3 was selected. Finally, the lower part of the spring was fixed. A 1D connector of the type RBE2 was added, with the nodes at the top plane of the plate as target nodes, to facilitate extraction of data. An enforced displacement constraint of -15 mm in the z-direction was finally applied on the source node of the 1D connector. This was done in order to simulate the compression of the plate.

The solver 601 was used for the simulation, with a solution time of 3 seconds and 30 time steps. The parameter ”Large displacements” was selected. The final setup is displayed in Figure 4.5

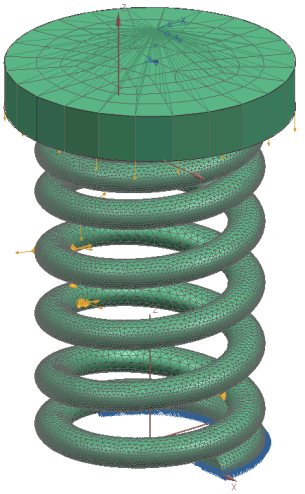

**Figure 4.5:** Simulation of the spring stiffness.

In Figure 4.6, the force/displacement curve from this analysis is displayed together with the measured force/displacement curve of the physical spring. Both the slope and the values of the force/displacement curve for the modelled spring, are representative of the ones obtained from the testing of the physical spring. The modelled spring should therefore be a good representation of the physical spring in terms of stiffness, geometry, mass and Young's Modulus.

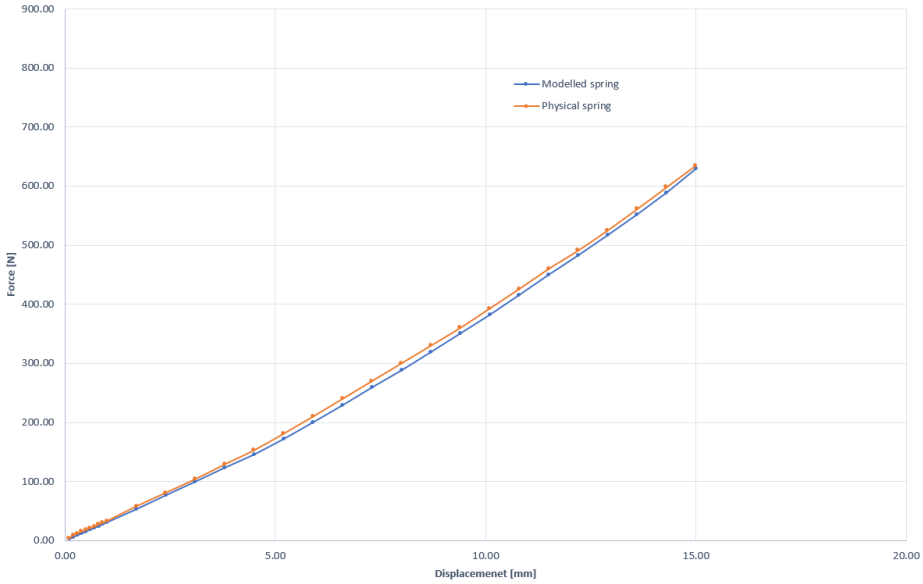


**Figure 4.6:** Force/displacement diagram.

## 4.2 Camshaft CAD Model and Mesh

In order for the simulation of the valve spring during load to be accurate, a good representation of the camshaft is crucial. The exhaust cam was therefore scanned using a 3D scanner, so that the cam profile could be accurately represented. A total of 1988 data points were used to capture the shape of the cam shaft. To generate a 3D-model of the camshaft from the data points, the function "fit curve", with "fit spline" was used in Siemens NX. The method "Degree and tolerance" was selected, and finally a spline with the following parameters was generated:

| Cam shaft | |
|---|---|
| Parameter | Value |
| Spline degree | 13 |
| Number of Poles | 709 |
| Number of Segments | 696 |
| Maximum Error | 0.00160 |
| Average Error | 0.00027 |

**Table 4.2:** 3D-model camshaft parameters.

This was then used to make the model of the cam shaft. In order to be able to use CHEXA(8) elements, the camshaft was meshed as two separate bodies, one for the shaft and one for the lobe. Element sizes of 2 mm and 2.5 mm respectively were used. The gliding surface of the lobe was also meshed with a surface mesh of the type CQUAD4. An element size of 3 mm and a thickness of 1 mm was used for this mesh. This was done in order to reduce the DOF of the nodes. The two bodies were connected using mesh mating. Finally, an RBE2 element was connected to the rotation surface of the cam. The FE-model is shown in Figure 4.7.

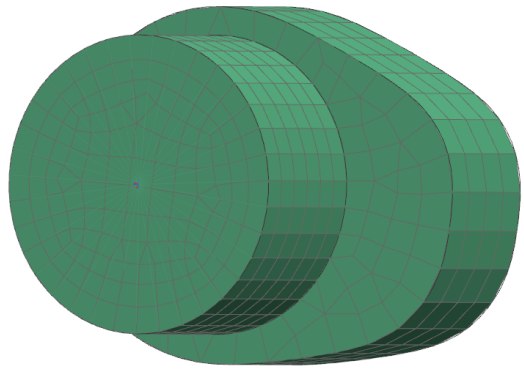

**Figure 4.7:** Meshed CAD model of the exhaust cam shaft.

### 4.2.1 Lift curve from cam shaft

Multiple ways of extracting the lift curve were considered. First, the built in motion application in Siemens NX was used to make a virtual cam reader as seen in Figure 4.8. By the use of 3D contact between the camshaft and the cam reader, a cam curve was obtained. However, the results obtained from this method are not satisfying as the accuracy is too poor. The resulting curve is shown in Figure 4.9.

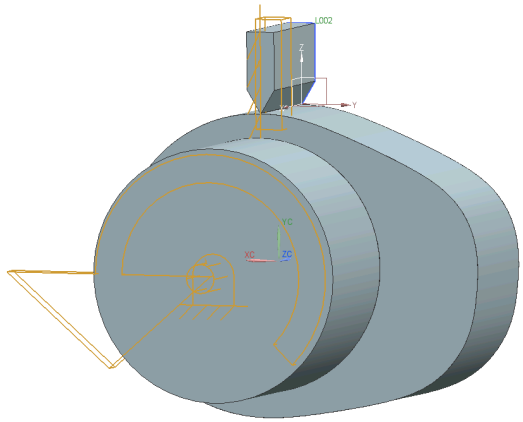


**Figure 4.8:** Virtual cam reader setup in NX.

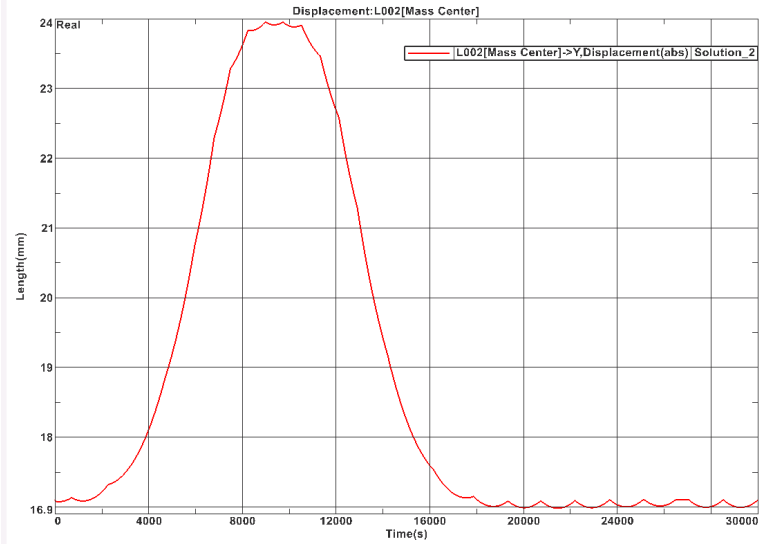


**Figure 4.9:** Cam curve obtained from the virtual cam reader setup in NX.

Consequently, a second way of obtaining the cam curve was evaluated. Each of the data points describing the shape of the cam profile were imported to Matlab, and a script was used to calculate the radius and the corresponding angle of rotation at each of the points. The curve shown in Figure 4.10 was finally obtained.

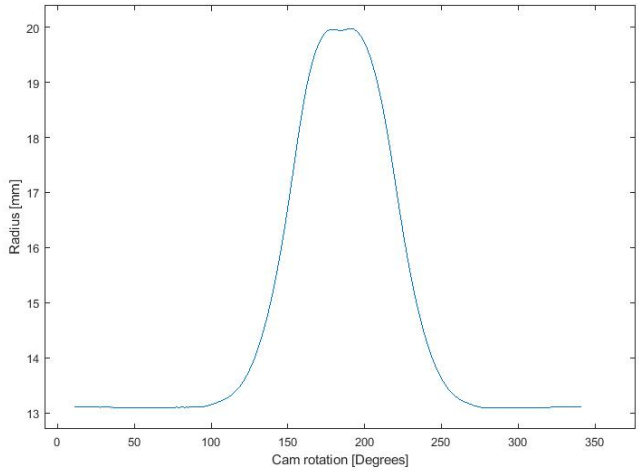


**Figure 4.10:** Exhaust cam profile.

## 4.3 Rocker Arm

The rocker arm is acting as a lever between the camshaft and the valve. In an engine with a Dual Overhead Camshaft (DOHC) like the Honda CRF250R, the rocker arm is pivoting around the end point. The valve on which the rocker arm is acting is located on the opposite end, at the rocker arm tip. Finally, the camshaft is located along the topside of the rocker arm, between the pivot point and the valve. The valve clearance between the rocker arm and the valve stem is set to 0.28 mm for the exhaust valve on the 2013 model, and is assumed to be the same for the 2018 model.

### 4.3.1 Rocker Ratio

Depending on the placement of the cam shaft, the rocker will have a rocker arm ratio. This ratio is usually defined as ”the ratio of valve lift to cam lift”, and it determines the actual amount of valve lift. Because the valve lift is affected by this ratio, the speed, acceleration and jerk of the valve will be affected as well.

### 4.3.2 True Rocker Ratio

The rocker ratio will be varying over the time of the valve lifting event. This is due to the fact that the rocker arm is pivoting around a given point. As a result, the rocker arm tip

will be moving on an arc around this pivoting point, while the valve stem is moving in a linear motion. Finally, the contact point between the camshaft lobe and the rocker will constantly be changing during the valve event.

### 4.3.3 Rocker Arm CAD Model and Mesh

The rocker arm was modelled based on pictures of the actual part, hence the accuracy is limited. It was also meshed using CHEXA(8) elements with an element size of 2 mm. Again, the gliding surface of the arm was meshed with a surface mesh of CQUAD4 with an element size of 2 mm and a thickness of 1 mm. Finally, two RBE2 elements were connected, one on each side of the pivot axle. The meshed part is shown in Figure 4.11.

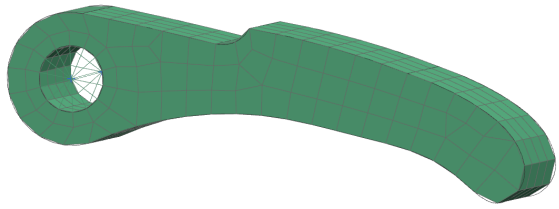

**Figure 4.11:** Meshed CAD model of rocker arm.

## 4.4 Valve Retainer CAD Model and Mesh

The valve retainer was also modelled based on pictures of the part. As the geometry of this part does not effect the operation of the valve spring itself, the part is not considered to be of great importance for the accuracy of the analysis to be satisfying. The only parameter actually influencing the result is the weight of the part, as this will oscillate together with the spring.

It was meshed as two separate bodies using CHEXA(8) elements with an element size of 3 mm and 2 mm for each of the parts. Mesh mating was used to connect the two parts. Finally, three RBE2 elements were connected, one along each of the edges. The final meshed part is shown in Figure 4.12.

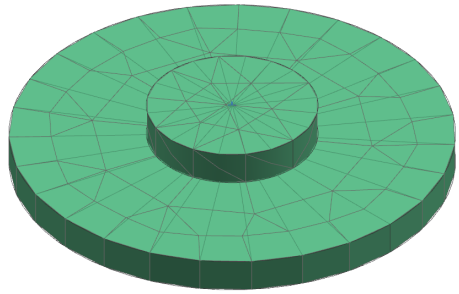

**Figure 4.12:** Meshed CAD model of valve retainer.

## 4.5 Eigenfrequencies

The 2018 Honda CRF250R has a max RPM of 14500, something that corresponds to a frequency of 120,83 Hz at the camshaft, when the gear ratio between the crankshaft and the camshaft of 2:1 has been taken into account. The valve springs have a tendency to fail at engine speeds close to maximum RPM. Therefore it has to be investigated whether the springs have any eigenfrequencies in close proximity to 121 Hz. If that is the case, this might cause resonance problems, eventually leading to the failure of the springs.

## 4.6 Valve Lift

The actual movement of the valve, the valve lift, is dependent on how the camshaft and the rocker arm is working together. In Figure 4.13 the actual valve lift (in red) is shown together with the lift generated by the cam profile (in blue). The curve of the actual valve lift was generated numerically in Matlab using the cam profile as input. The contact point of the camshaft and rocker arm at each point of cam rotation is calculated. From this, the amount of rocker arm pivot is given. Accordingly, the valve displacement can be extracted. As seen from the figure, the rocker arm makes the valve lift higher, as well as providing a steeper lift curve. The maximum valve lift of the 2018 model is 9.5 mm.

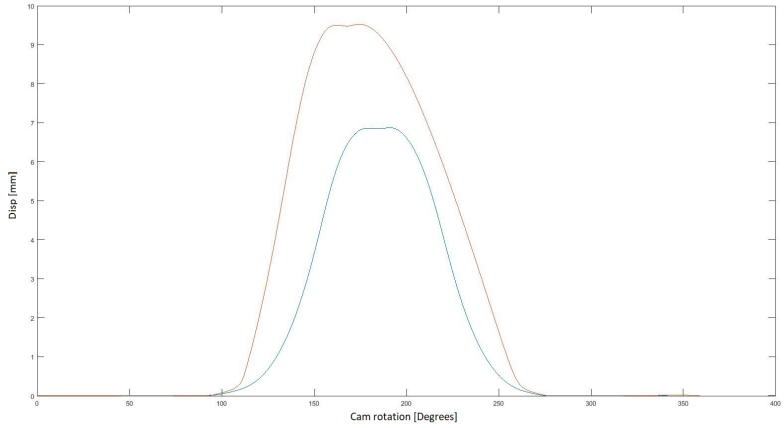


**Figure 4.13:** Exhaust cam profile and modified curve from rocker arm.

## 4.7 Stress Analysis in NX

A stress analysis of the spring during compression is performed using Siemens NX. The advanced nonlinear solver 601 is used in order to capture the geometric nonlinear effects from the change of the stiffness properties as the spring is deformed. This solver also allows for simulation of contact parameters as the spring coils are coming in contact during the deformation.

A 1D connection of the type RBE2 is added to the top surface of the spring in order to simulate the valve retainer. Apart from this, it is constrained as described in section 4.1.3. The final setup is shown in Figure 4.14.

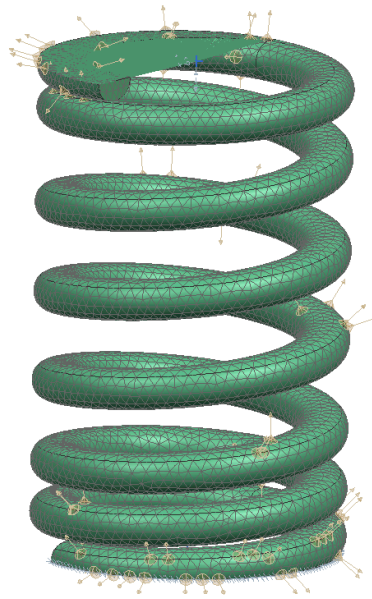

**Figure 4.14:** Setup of stress analysis in Siemens NX.

## 4.8 Dynamic Analysis in FEDEM

A dynamic analysis of the valve train assembly is conducted using FEDEM. The FE models of the parts are extracted from Siemens NX as Nastran Bulk Data Format (.nas) files, and imported to FEDEM.

### 4.8.1 Model Setup

The FEDEM model consists of the following five parts, with the corresponding colours and constraints, shown in Figure 4.15:

- Exhaust cam in turquoise: Constrained by two revolute joints at the camshaft, one at each of the RBE2 elements connected to the shaft.
- Rocker arm in blue: Constrained by two revolute joints connected to the two RBE2 elements at the pivot point.
- Valve retainer in yellow: Constrained by a fixed joint connecting the slave node of one of the valve retainer RBE2 elements to the RBE2 element at the top of the valve

spring. A free joint with displacement allowed in Tz is added. This is connected to the bottom of the valve retainer, and attached to the ground plane, in order to simulate the stabilising from the valve stem. Rz is also kept free in order to allow rotation of the valve during operation.

- Valve spring in green: Connected to the valve retainer at the top. Additionally, it is constrained by a free joint with Tz and Rz free, defined by a slave node connected at the RBE2 element at the bottom of the spring, and the master node connected to the ground plane. Again, Rz is kept free in order to allow rotation of the spring.
- Valve: Simulated as a generic part connected to one of the RBE2 elements at the valve retainer with a fixed joint. This is done as the only factor influencing the analysis is the mass of the valve. As the valve of the 2018 Honda CRF 250R is made of titanium, the weight is set to 60 g.

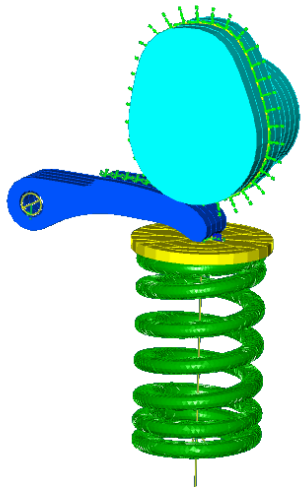

**Figure 4.15:** Model setup in FEDEM.

### Cam Joint

A crucial part of the simulation is the way the contact between the cam and the rocker arm is modelled. This is done using the cam joint function. In FEDEM, a cam joint consists of a cam curve and a slave triad. The cam surface is defined by a curve consisting of three-point circular arcs, where each arc is defined by the location of three master triads [Fedem Technology AS (2016b)]. The cam curve in this model is constructed from a total of 23 master triads positioned along the cam surface. The triads are positioned so that positive x-direction is normal to the surface, as seen in Figure 4.16. 11 separate cam joints, each with one single slave triad, are constructed in order for the rocker to precisely

follow the movement of the cam shaft. The slave triads in the cam joint are following the translation in the x-direction of the master triads. This is achieved by defining a spring-damper relation with a stiffness of $k = 10^7 N/m$ for negative x- values and 0 for positive. This is done so that the slave triads are effected by the master triads, but only when one of the slave triads is in direct contact with the cam curve. As each cam joint only recognises the connected slave triad, and not the surface of the part, adding more slaves will increase the accuracy of the follower cam. For this simulation, 11 cam joints are sufficient in order to have a satisfying representation of the rocker arm and cam profile contact.

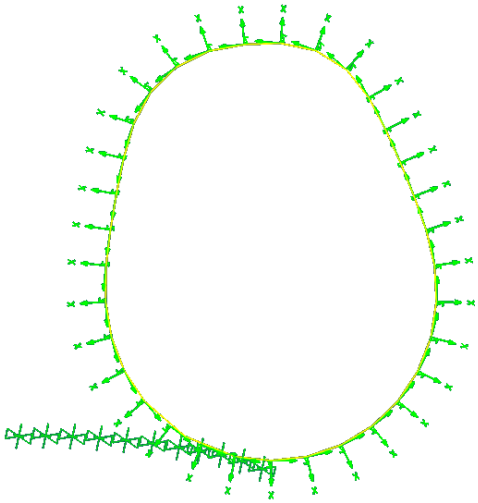

**Figure 4.16:** Cam joint.

### Simulations Steps

- Initial spring compression: The valve spring will be compressed during installation in order for the valves to seat properly during the closing operation. A precompression of approximately 15% of the total spring length is reasonable, [Jr. and Rethwisch (2000)]. This means that a total initial compression of 5.5 mm should be applied to the spring. This is done by adding a prescribed displacement of 5.5 mm in the z-direction to the free joint, which is acting as the spring support, at the bottom of the spring. The compression is added linearly within the first second of the simulation.

- Cam rotation: In order to simulate the rotation of the cam shaft, a rotation is added to one of the revolute joints connected to the cam. This is done using the limited ramp function with a total of one revolution. The rotation starts one second into the simulation, right after the precompression. A rotation of 1 Hz is used.

### 4.8.2 Structural Damping

In order to have a more stable simulation, and remove numerical noise, structural damping is added to the model. Rayleigh Viscous Damping (mass and stiffness proportional) is used in order to calculate the damping for each of the parts. In order to calculate the mass proportional and stiffness proportional damping, the two first eigenfrequencies of the reduced system are extracted for each of the parts. This can be seen in Table 4.3. A damping ratio of 3 % of critical damping was added to all of the parts:

| Part | Mode 1 | Mode 2 | Mass Proportional | Stiffness Proportional |
|---|---|---|---|---|
| Spring | 451 Hz | 518 Hz | 90.8 | 9.9E-06 |
| Retainer | 57450 Hz | 77829 Hz | 12454.1 | 7.1E-08 |
| Rocker | 19368 Hz | 23651 Hz | 4012.2 | 2.2E-07 |
| Exhaust cam | 49651 Hz | 58756 Hz | 10139.9 | 8.8E-08 |

**Table 4.3:** The two first free-free component modes are extracted for each of the reduced parts, and corresponding mass proportional and stiffness proportional damping are calculated using the equations in 3.7

Chapter 5

# Analysis

The first part of the analysis, conducted only on the exhaust valve spring, was performed during the semester project ”High performance cam profile design and optimization” written by the signatory. As this spring still is the component to be evaluated in this masters thesis, the results from these analyses are also included in this paper. Although these are conducted on a slightly different meshed spring, this should not have a relevant impact on the results.

## 5.1 Free-Free Eigenfrequency Analysis

Initially, an eigenfrequency analysis of the spring itself is performed. This analysis is conducted on the spring with the material properties of the NX library material ”Steel”. The free-free analysis is very simplified compared to the real scenario because the spring is neither precompressed, as it will be during normal operation, nor constrained in the same way. As described in section 3.6.2, this means that both the natural frequency and the mode shapes will change in the real scenario. The analysis only considers the spring as an independent object. This is done in order to investigate the range of natural frequencies of the spring alone, something that can be useful when comparing the results to the more realistic scenario later.

”The usual first step in performing a dynamic analysis is determining the natural frequencies and mode shapes of the structure with damping neglected. These results characterise the basic dynamic behaviour of the structure and are an indication of how the structure will respond to dynamic loading.”,[Siemens AG (2014a)].

### 5.1.1 Results

The 6 first modes extracted from the analysis are the rigid body modes. They are a result of the spring being unconstrained, and consequentially there exists one mode shape for each degree of freedom. These frequencies are not interesting and are therefore not taken into account. The next four eigenfrequencies are in the range 450-573 Hz. In Figure 5.1, the mode shapes for each of the four first eigenfrequencies of the valve spring are displayed. It should be mentioned that the mode shapes are relative quantities, hence they do not represent the actual dynamic response of the spring. In order to determine the magnitude of the dynamic response, the structural loading has to be taken into account as well.

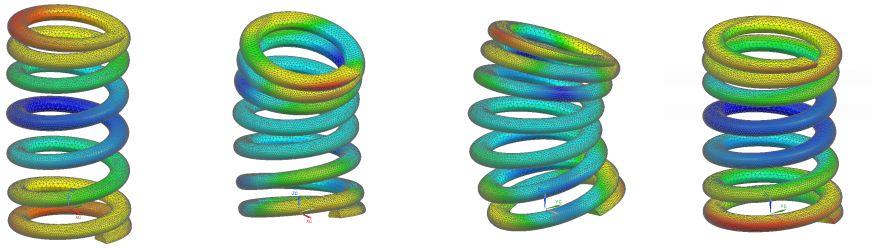

**(a)** 450.05 Hz **(b)** 514.503 Hz **(c)** 515.933 Hz **(d)** 573.66 Hz

**Figure 5.1:** The mode shapes of the exhaust valve spring at different frequencies.

## 5.2 Precompressed Eigenfrequency Analysis With Temperature Dependent Material

A valve spring will be compressed during installation in order to have a satisfying closing of the valve. A compression of approximately 15% of the total spring length is reasonable, [Jr. and Rethwisch (2000)]. Accordingly, a compression of 5.5 mm is applied to the top of the spring during the analysis. The material temperature is set to 20°C.

Finally, the bottom part of the spring is fixed. The setup can be seen in Figure 5.2.

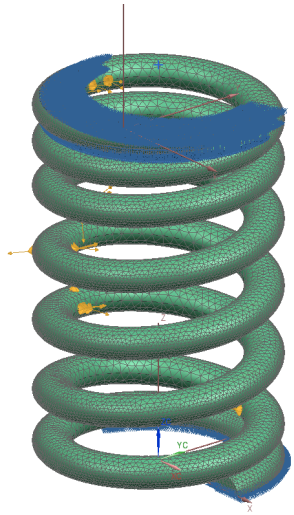

**Figure 5.2:** Eigenvalue analysis for the valve spring when precompressed.

### 5.2.1 Results

Now that the spring is completely constrained, the rigid body modes do not exist. In Figure 5.3, the first four mode shapes and their corresponding eigenfrequencies are displayed. As in the previous simulation, the mode shapes are relative quantities. As expected, the first four eigenfrequencies are measured to be slightly higher in this analysis, as the spring is now stiffer. This is reasonable, as it is constrained in both ends, and the total length of the spring is decreased due to the precompression. The first four frequencies are now in the range of 503-665 Hz, well outside the driving frequency imposed by the camshaft of 121 Hz. Finally, the shape modes of the spring are different, as the new constraints restrict the movement of each of the spring ends. However, the way each of the spring ends are constrained is not a completely accurate representation. This is because the spring during operation is only constrained by the engine head and the valve retainer, something that allows the spring to rotate. On the contrary, it is completely fixed in the simulation. Finally, the increased temperature in the spring during operation is not taken into account.

According to Jr. and Rethwisch (2000), a typical exhaust valve spring will have a temperature of 80°C during normal engine operation, yet this can be even higher under max load. Therefore, this analysis is also conducted with the elevated material temperatures of 80°C, 120°C and 160°C. Figure 5.4 displays the eigenfrequencies of the first four mode shapes for the valve spring at different temperatures. As expected, the stiffness of the spring will decrease as the temperature increases. This will give lower eigenfrequencies, while the mode shapes will stay the same.

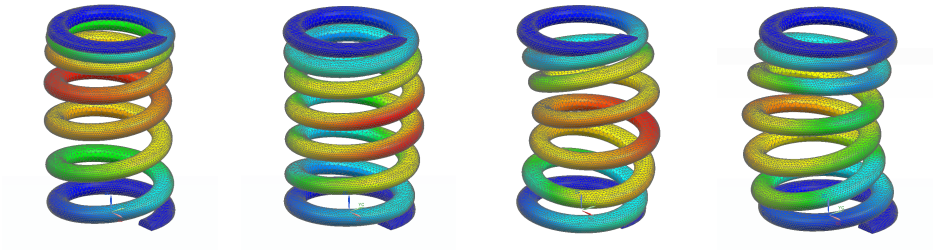

**(a)** 503.428 Hz **(b)** 633.16 Hz **(c)** 657.058 Hz **(d)** 665.178 Hz

**Figure 5.3:** The mode shapes of the precompressed exhaust valve spring at different frequencies.

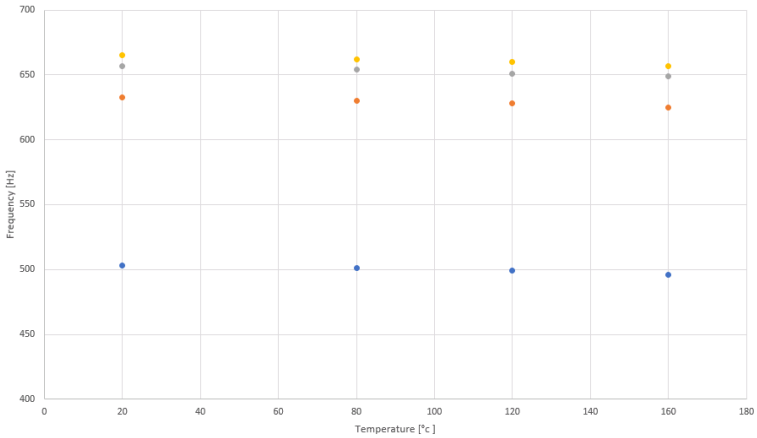


**Figure 5.4:** First four eigenfrequencies at different temperatures.

Even with these increased temperatures, the lowest eigenfrequency of the spring is 496 Hz at a temperature of 160 °C. This is far from the driving frequency of the camshaft at max RPM of 120.83 Hz, and thus indicates that resonance should not be a problem. However, some of the mass from the valve and the valve retainer will follow the spring movement, something that will have an impact on the eigenfrequencies of the spring.

## 5.3 Eigenfrequency Analysis with Temperature Dependent Material and Additional Mass

Because some of the mass from the valve and the valve retainer will be oscillating together with the spring, impacting the eigenfrequencies, this extra mass should be taken into account.

In order to simulate this, a simulation object of the type ”Non-Structural Mass” is added to the top of the spring. For this analysis, the spring is only fixed at the bottom. As the non structural mass requires target elements of the type 2D, the spring is partitioned as three parts: One for each of the ends, and one for the middle part. All the parts are meshed using the same conditions as before, but also a 2D mesh of the type CQUAD4 is added to the top plane, with an element size of 1 mm. Finally, mesh mating is used in order to connect the separate bodies. This setup is seen in Figure 5.5,

The Non-Structural mass is added as a distributed mass on the elements at the top face of the spring. The simulation is performed with a material temperature of 80 °C.

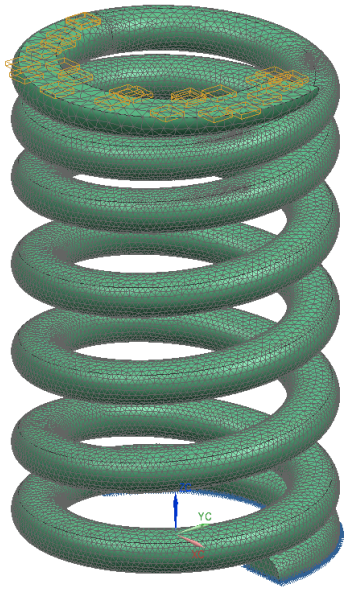


**Figure 5.5:** Eigenvalue analysis for the spring with additional mass acting on the top face of the spring.

### 5.3.1 Results

As the mass of the valve and the valve retainer is unknown, the analysis is performed multiple times with varying mass added to the spring. The eigenfrequncies obtained are displayed in the Figure 5.6. It is clear that the eigenfrequencies are lowered as the the distributed mass is increased. This analysis indicates that the spring might have multiple eigenfrequencies in close proximity to the excitation frequency at max RPM of 121 Hz, depending on the magnitude of the additional mass oscillating with the spring. It should be specified that the way this analysis is conducted does not allow for the top of the spring

to be constrained as in the engine. This results in a lower overall stiffness, contributing to lowering the eigenfrequencies.

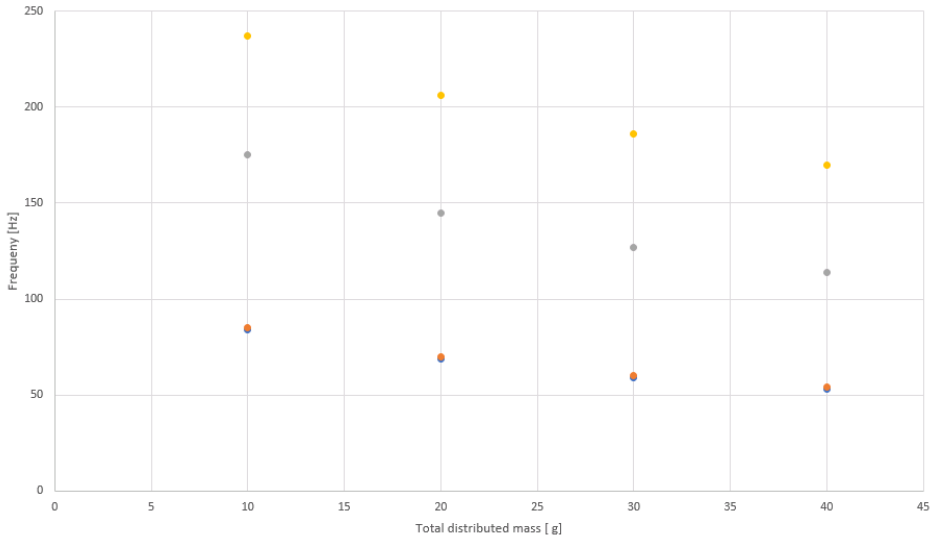


**Figure 5.6:** First four eigenfrequencies for the spring with additional mass in the range of 10-40 g.

## 5.4 FEDEM Simulation

The main purpose of the simulation in FEDEM is to investigate how the spring behaves during the realistic loading scenario in the engine. In this simulation, the different parameters discussed in the previous analyses are combined and taken into account. Because the whole valve train is simulated, the mass of the parts oscillating with the spring, namely the valve and valve retainer, are also included. Finally, the actual lift curve generated by the camshaft and rocker arm working together is the one generating the compression of the spring. The interesting output from this analysis is the eigenfrequencies and the system modes of the valve train at different stages of compression during normal operation. This allows for an investigation of the relevant system modes affecting the valve spring, and an evaluation of the corresponding eigenfrequencies. Finally, this might establish whether resonance in the valve springs is possible.

In Figure 5.7, the FEDEM model during simulation is displayed. This figure shows the simulation after 1.4 seconds, when the spring is at its most compressed. The simulation looks reasonable at this stage. The cam joint is well modelled, as the rocker arm follows the cam profile well, without intersecting, or losing contact with the cam lobe.

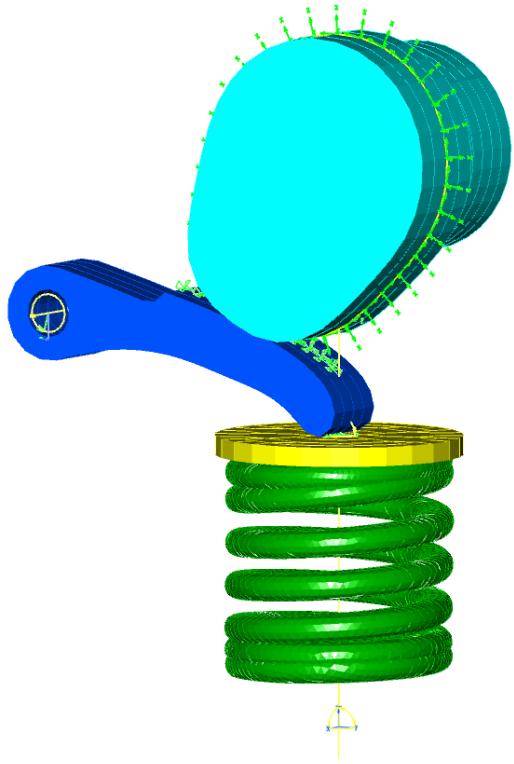

**Figure 5.7:** Running simulation after 1.4 sec at maximum spring compression.

### Results

The valve retainer moves from 0.0984 m to 0.0894 m in the global z-direction during the simulation, as seen in the Figure 5.8. This corresponds to a total compression of 9 mm in the spring. The compression is a result of the rotation of the camshaft generating a pivoting movement of the rocker arm as the cam lobe is sliding along the contact surface of the rocker arm. As the spring is compressed, the valve is lifted to a maximum valve lift of 9 mm. The actual valve lift of the Honda CRF 250R 2018 model is listed as 9.5 mm, this corresponds to an error of 5.56 % in the simulation. This error is due to an imprecise modelling of the rocker arm and/or small inaccuracies in the camshaft, rocker arm and valve assembly.

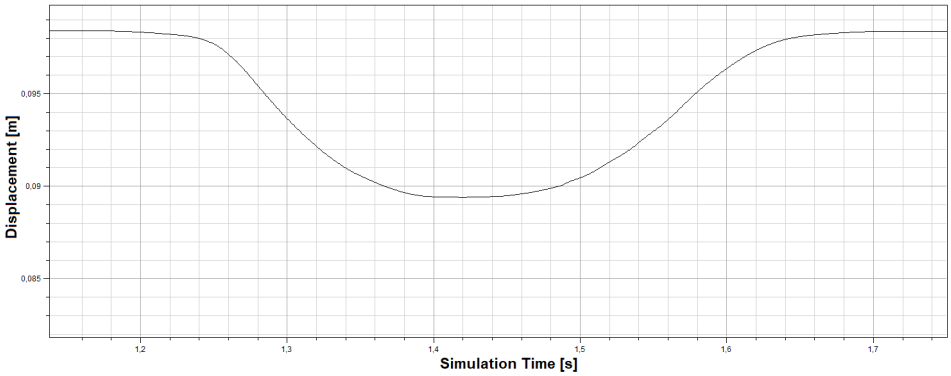


**Figure 5.8:** Displacement of the top of the spring.

FEDEM does not include a way to simulate self contact within a part. Therefore, this analysis does not take self contact between the individual spring coils into account. This will effect the stiffness of the spring at the fully compressed stage of the cycle, and also the stress levels generated in the spring. The first two coils from the top, and the last three coils will be in contact at this stage, as seen in Figure 5.7. Even though the coils in the simulation are evidently intersecting, the overall stiffness of the spring is not affected. As a result, the simulated spring will have a lower overall stiffness, as well as reduced stress levels in the spring coils at this stage of the simulation. The resulting maximal stresses obtained in the middle coils are at the magnitude of 1.19 GPa, considerably lower than the ones later found in the stress analysis in Siemens NX in section 5.5. However, as seen from the Figure 5.9, the maximal overall stresses can be found at the region at the top of the spring, in the transition from the flat end to the spring coil, and is of approximately 6.36 GPa. This stress level is not realistic, as in FEDEM this part of the spring has to transfer the whole load to the rest of the spring, while in the real scenario, it will be distributed to the second coil coming in contact during compression. This effect is captured in the stress analysis in Siemens NX, and is therefore discussed further in that section.

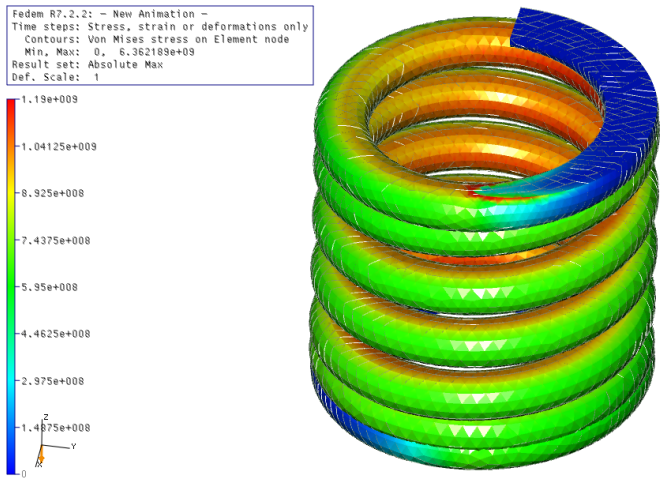


**Figure 5.9:** Elemental Von-Mises stress in spring when fully compressed at 15 mm of compression during simulation.

The Graph 5.10 shows the contact force between the rocker arm and the retainer. As expected, it is steadily increasing as the spring is precompressed during the first second of the simulation. In the following 0.1 second, the curve has some extreme values as the camshaft starts to rotate. By looking at the animation from this part of the simulation, it is clear that as the camshaft starts to rotate, some quivering is generated in the rocker arm, causing the jittering in the graph. This is probably a result of the master triads of the camshaft starting to move in respect to the slave triads of the cam joints, resulting in a sudden peak in the stiffness of the spring function controlling the contact behaviour in the cam joint. These extreme values are therefore considered to be noise, and not taken into account in the further analyses.

From then on, the curve is smooth throughout the simulation, with a peak as the spring is fully compressed. This is expected, as the spring force is increasing while the spring is compressed. Because the interesting part of the simulation is during the compression of the spring, the noise in the beginning of the camshaft rotation is not considered a problem for the accuracy of the results. The maximum contact force between the retainer and the rocker arm, excluding the noise as the rotation of the camshaft starts, is of approximately 417 N.

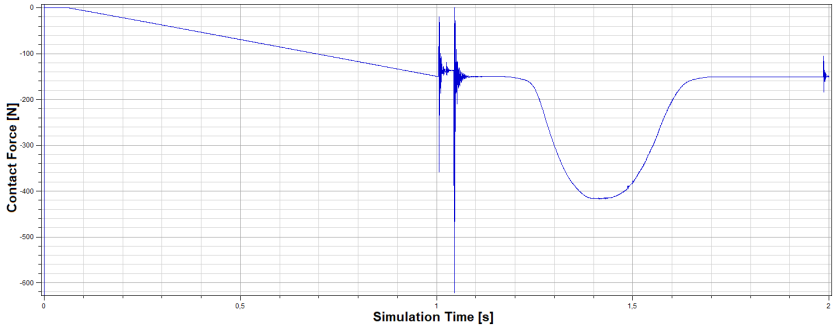


**Figure 5.10:** Contact Force between retainer and rocker.

The strain energy in the spring is shown in the graph in Figure 5.11. Again, the graph is smooth, except for the part where the cam rotation starts. The peak strain energy stored in the spring at maximum compression is at approximately 2.9 J.

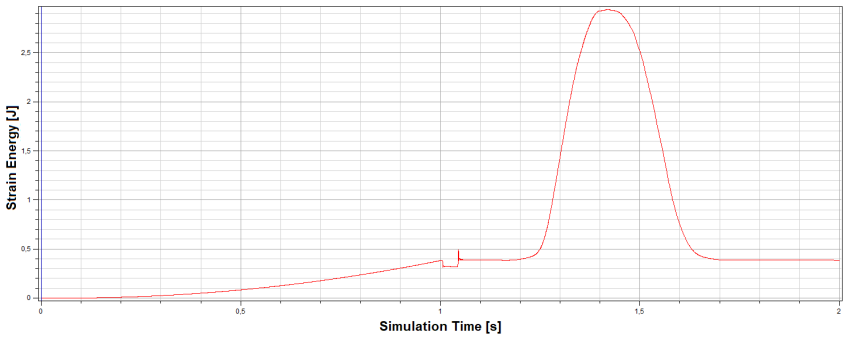


**Figure 5.11:** Strain energy in the spring.

The four first eigenfrequencies and the corresponding eigen modes of the system were extracted running a mode shape recovery analysis. The eigenfrequencies are displayed in the Figure 5.12. The red line shows the first eigenfrequency of the system at just above 0 Hz. This frequency is a result of the spring being allowed to rotate about the z-axis. The second system eigenfrequency is given by the black line. This frequency is not relevant, as the corresponding system mode shows that this frequency is only effecting the valve retainer. Finally, the third and fourth system eigenfrequencies, displayed by the blue and green line respectively, are both acting on the spring. They are stable at 570 Hz and 657 Hz after the initial compression of the spring, and then drops to 497 Hz and 572 Hz during the simulation when the spring is fully compressed. In Figure 5.13 and 5.14, the mode shapes of the third and fourth system modes are displayed in three steps in order to show

how the spring behaves as it is oscillating at these frequencies.

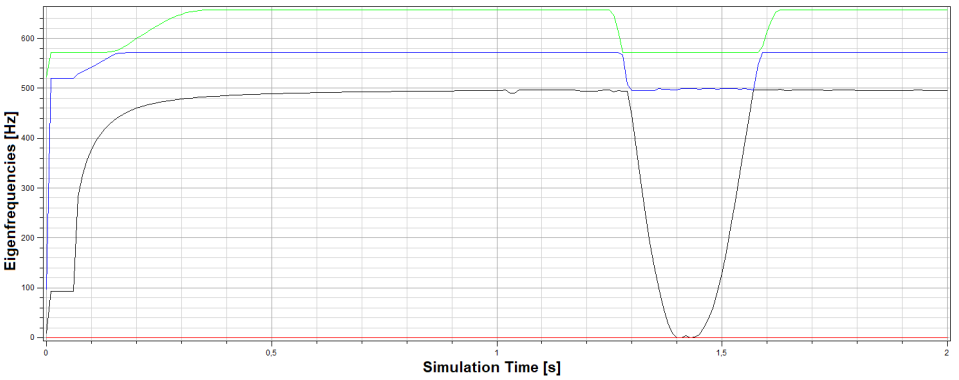


**Figure 5.12:** Eigenfrequencies of the system as a result of simulation time.

**(a)** Step 1 **(b)** Step 2 **(c)** Step 3

**Figure 5.13:** The third system mode shape of the valve spring when the spring is fully compressed after 1.4 seconds with an eigenfrequency of 496.99 Hz.

**(a)** Step 1 **(b)** Step 2 **(c)** Step 3

**Figure 5.14:** The fourth system mode shape of the valve spring when the spring is fully compressed after 1.4 seconds with an eigenfrequency of 571.58 Hz.

## 5.5 Stress Analysis in Siemens NX

The purpose of the nonlinear stress analysis in Siemens NX is to evaluate the maximal stress levels in the valve spring at the stage of the cycle where it is at its most compressed. This data can later be used in the fatigue analysis in order to establish the service life of the valve spring.

### 5.5.1 Results

The elemental stress of the spring can be displayed as both average nodal stress and average elemental stress. Figure 5.15a shows the elemental stress in the spring calculated using Von-Mises. A maximum of approx 1648 MPa is generated in the spring when it is fully compressed. The maximum stress is occurring in the inner part of the middle coils of the spring. This is reasonable, since a helical compression spring submitted to an external compressive force will generate torsional stresses in the active spring coils, as these can be simplified as straight torsion bars. Because the total shear stress in the inner coils will be the sum of both the direct shear stress and the torsional shear stress, the stress levels will be the greatest in this part of the coil.

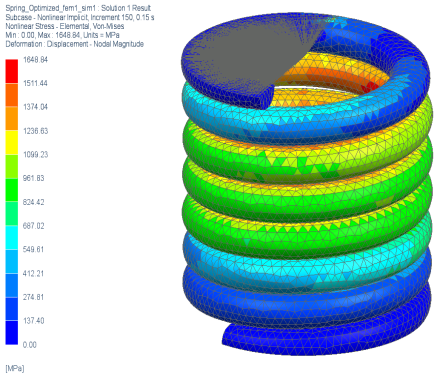


**(a)** Fully compressed spring, 15 mm of compression. Elemental stress, Von-Mises.

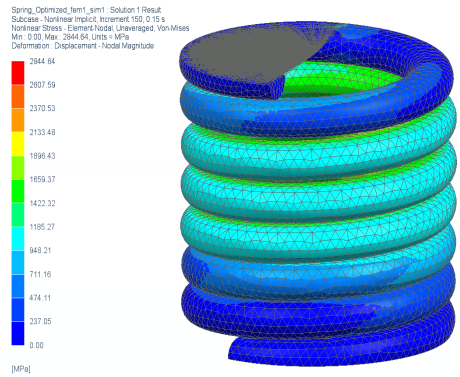


**(b)** Fully compressed spring, 15 mm of compression. Nodal stress, Von-Mises.

**Figure 5.15:** Von-Mises stress.

Figure 5.15b shows the nodal stress, also calculated using Von-Mises. The stress levels in the middle coils are still within the same range. However, the maximal stress level occurring in the model is now significantly higher, at approximately 2800 MPa. This can be explained by looking at Figure 5.16 and the theory behind nodal and elemental stress calculations.

Figure 5.16 shows the top part of the spring where the flat end-coil translates into the constant spring coil. Because the RBE2 element is connected to the flat surface on the spring end, the nodes on this surface experience higher stress than the surrounding nodes. The gaussian points in each element is used to calculate the stress at the element nodes. When multiple elements share one node, the nodal stress of that node will be the average of the nodal stress calculated for the specified node in each elements. For the elemental stress however, the average of the nodal stress calculated for one element, based on the gaussian point, is used to calculate the elemental stress. Because of the way the RBE2 element is connected to one of the nodes at this specific point, the stress at this node is higher than what would be expected, resulting in a nodal stress of approx 2800 MPa in this area. For the elemental stress however, the extreme value of this one node is averaged out by the other nodes of the element, resulting in a smaller error.

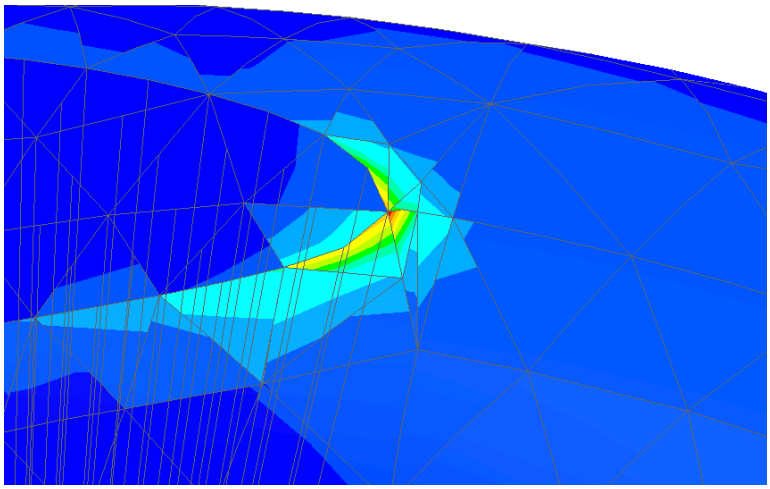

**Figure 5.16:** Problem area for the nodal stress calculation.

The maximum shear stress obtained by this analysis can be compared with the stress obtained by a simple estimate using the equations introduced in 3.4.2. Using the parameters W = 644 N (the measured compression force from the simulation in Siemens NX), D = 20 mm and d = 3.4 mm (the average diameter of the elliptical cross section), a maximum shear stress of 1049 MPa is estimated. However, as seen from the legend in Figure 5.17a, the maximum shear stress in Siemens NX is measured at 948 MPa. As these values are of the same magnitude, this indicates that the result obtained from the analysis is reasonable.

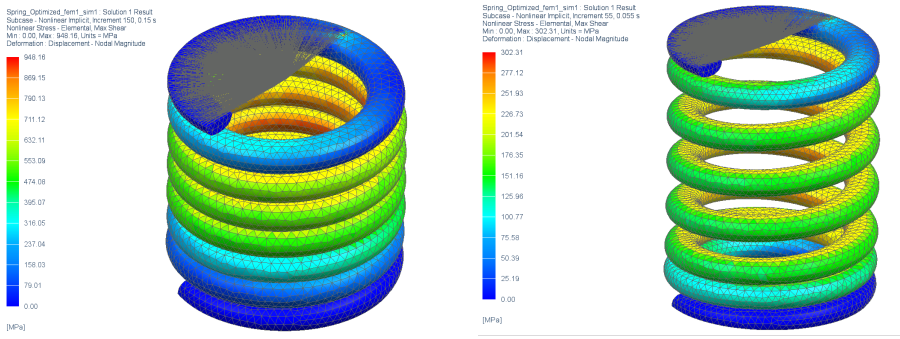


**(a)** Fully compressed spring, 15 mm of compression. Shear stress, elemental.

**(b)** Precompressed spring, 5.5 mm of compression. Shear stress, elemental.

**Figure 5.17:** Shear stress, elemental.

Initially, when the spring is precompressed, the shear stress in the middle coils of the spring is at 302 MPa. See Figure 5.17b.

## 5.6 Fatigue Analysis

In order to investigate if failure due to fatigue is a problem for the valve springs, the S-N curves for the given material is necessary. The study conducted by C.Berger and B.Kaiser (2006) establishes the S–N curves for 10%, 50% and 90% failure probability for valve springs of the same material as the one assumed to be used for the 2018 Honda CRF 250R, but with a constant wire diameter of d = 2 mm. Both short term fatigue, $N = 10^7$, and long-term fatigue, $N = 1.2 \times 10^9$, is considered in the study. The experiments are performed with a stress range of R = 0.05 and a test frequency of f = 20 Hz.

### 5.6.1 Goodman Curves

Using the theory of Goodman diagrams as described in section 3.8, the alternating stress from the ”corrected stroke stress”, the mean stress and the UTS of the springs in the study, the endurance limit, $\sigma_e$, for each of the tests can be established. These values can be used to plot the Goodman diagrams for the valve springs of the 2018 Honda CRF 250R. By using the endurance limits found in the previous study, and the actual UTS of the valve springs in question, the Goodman lines can be constructed.

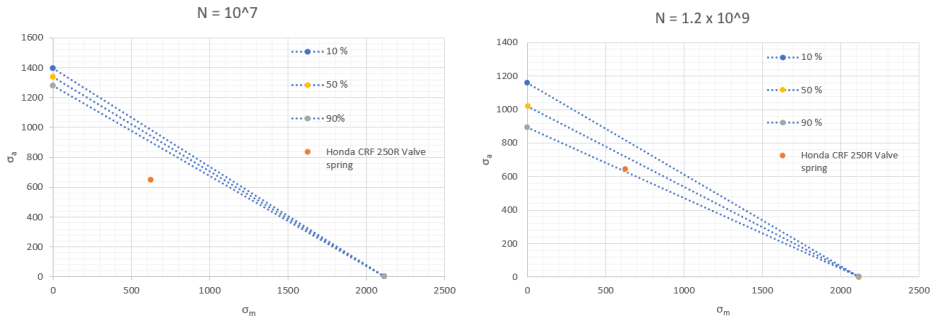


**(a)** Low cycle fatigue.

**(b)** Very high cycle fatigue.

**Figure 5.18:** The Goodman diagrams for different cycles. The lines represent the failure probability for each combination of stress amplitude and mean stress.

### Results

The stress amplitude and the mean stress for the valve spring are generated from the results obtained from the compression analysis in Siemens NX, with a $\sigma_{max} = 948MPa$ and a $\sigma_{min} = 302MPa$ for a compression of 15 mm and 5.5 mm respectively. This gives a $\sigma_{alt} = 646MPa$ and a $\sigma_m = 625MPa$. The results are displayed in Figure 5.18.

In the situation with low cycle fatigue in Figure 5.18b, fatigue does not seem to be a problem, as the valve spring is well below the Goodman line representing a 10% failure probability. In the very high cycle fatigue scenario of Figure 5.18a however, the valve spring lies between the Goodman lines representing a 10%, and a 50%, failure probability, indicating that fatigue at this cycle level is a possibility.

### 5.6.2 FEDEM

A virtual strain rosette has to be placed at the point of interest on the part in FEDEM, in order to obtain the stress input for the rainflow analysis. This is done by defining 4 FE nodes and a direction. The nodes defines a strain element in which the strain and stress is calculated at the centroid of the element, based on the deformation of the nodes [Fedem Technology AS (2016b)]. In order to capture the highest stress, it is placed on the inside of the middle coil, as shown in Figure 5.19.

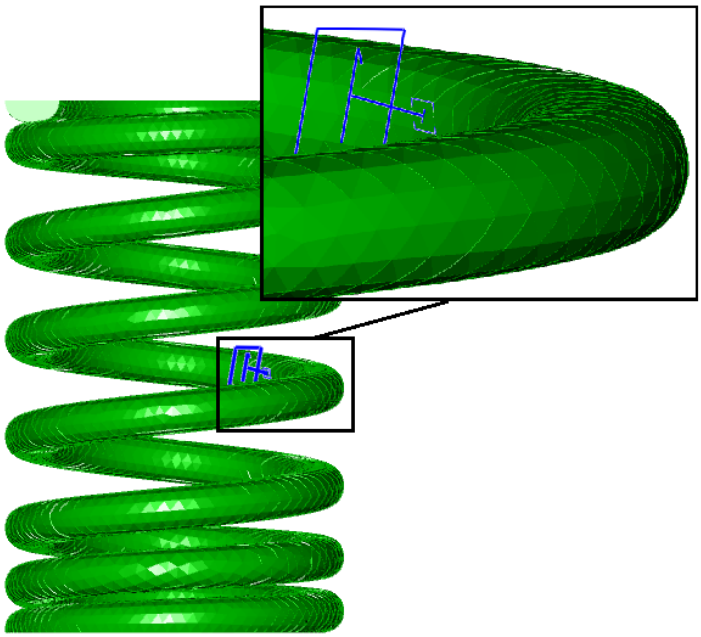

**Figure 5.19:** Location of the strain rosette on the valve spring.

#### Results

FEDEM includes a number of standard S-N curves from the DNV GL, RP-C203 standard. Because the already defined curves are only valid for steel with very different properties than the ones of the steel alloy in question, a S-N curve for the material of the valve spring first has to be defined. This is done by using the theory described in section 3.8.1. Empirical data on the fatigue behaviour is necessary to determine the design variables of the S-N curve. The data obtained in the study conducted by C.Berger and B.Kaiser (2006) is used for this purpose.

The calculated S-N curve is now defined by the following line segments:

- First line segment: $log(\bar{a}1) = 18.1471$ and $m1 = 3.85$
- Second line segment: $log(\bar{a}2) = 93.9848$ and $m2 = 29.52$

These two segments are defining the following S-N curve shown in Figure 5.20.

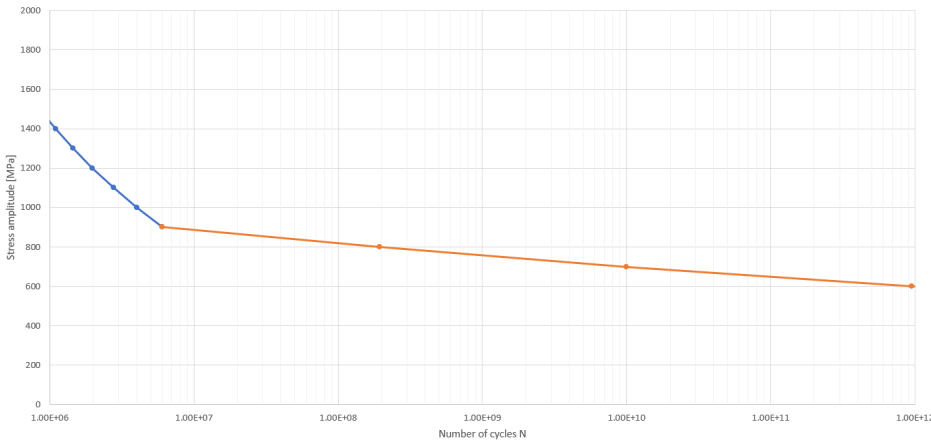


**Figure 5.20:** S-N curve for a 90% survival probability.

The stress tensor output from the strain rosette is shown in the Figure 5.21a, showing a maximum stress of 1.07 GPa, measured by the strain rosette. For the fatigue life calculation, only the time interval from 1.1 to 1.9 seconds is used in order to avoid any influence from the numerical noise at the first and last part of the rotation of the camshaft. The Figure 5.21b shows the corresponding rainflow for the simulation. This is obtained from the peak valley extraction, where a stress range threshold of 1 MPa is applied. Because the camshaft is only doing one rotation and the low stress amplitudes are filtered out, the rainflow is very simple, with just one tensile peak.

For this given stress output, the damage in the middle coil of the spring per cycle is calculated at $D = 5.16 \times 10^{-11}$, giving a corresponding $N = 1.94 \times 10^{10}$ cycles until failure. This is a considerable longer service life than what is suggested by the fatigue analysis based on the Siemens NX results. There might be multiple reasons for this. Most importantly, as discussed earlier, the spring in FEDEM is only compressed a total of 14.5 mm when at maximum compression. This will result in lower stress levels in the FEDEM simulation.

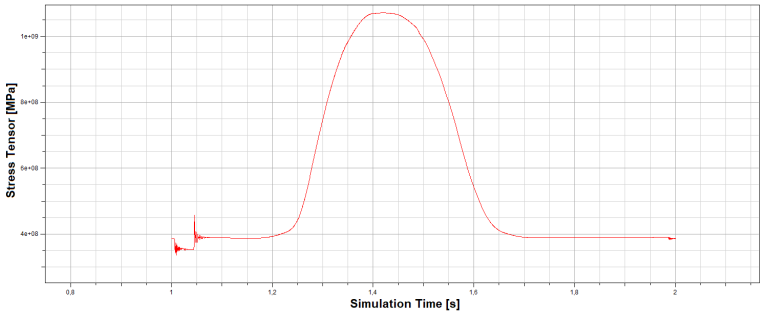


**(a)** Stress tensor output from strain rosette. [Pa]

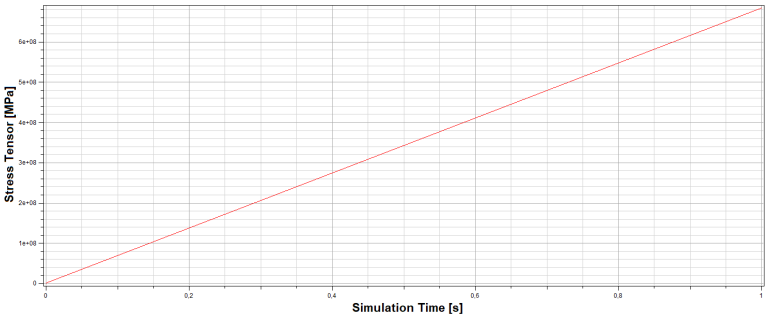


**(b)** Rainflow with a stress range threshold of 1 MPa.

**Figure 5.21:** Stress tensor and rainflow.

Chapter 6

# Discussion

The main objective of this masters thesis is to find the reason for failure in the high performance valve springs of the Honda CRF250R 2018 model. In order to do this, the complete valve train had to be reverse engineered. The accuracy of the modelled parts is important in order for the results from the analyses to be valid.

The measurements and comparison of the physical spring and the modelled spring corresponds well. Additionally, the force-displacement curve obtained from the nonlinear analysis performed to simulate the compression of the spring, and the force-displacement curve obtained from physical test of the actual spring, coincide well. Therefore, the modelled spring should be a good representation of the physical spring in terms of stiffness and behaviour during loading. This is important as the accuracy of all the other analyses rely on the spring being well modelled.

The camshaft is also assumed to be well represented as laser 3D scanners typically have an accuracy of 0.1 mm or less. Therefore, the data points used in Siemens NX to model this part are accurate. Combined with the reasonable high density of points, the model should be a good representation of the physical part.

For the other parts however, namely the rocker arm, valve retainer and valve, the accuracy is not in the same range. Because the parts could not be obtained, these parts are modelled from pictures of the actual parts, and it is therefore expected that the measurements might be deviating by multiple millimetres from the physical parts. As the only part with geometry effecting the analysis is that of the rocker arm, this should not have a substantial impact on the results of the dynamic simulation in FEDEM. However, it is reasonable to assume that the inaccuracy in terms of the slightly lower lift obtained in the dynamic analysis in FEDEM is a result of the rocker arm not being well represented. In terms of mass, all of the parts will influence the eigenfrequencies of the system. As the mass is calculated from

the CAD models and the material properties, some error will be present here.

The initial results of the free-free eigenvalue analysis of the spring indicates that eigenfrequencies of the spring is in the range of 450-574 Hz. The second analysis, where the spring is precompressed and completely constrained in both ends, shifts the eigenfrequencies upwards compared to the results obtained from the initial analysis. This is reasonable, as the spring is both stiffer, as it is constrained in the end points, but also shorter due to the compression. The first 4 normal frequencies are now in the range of 503-665 Hz. These frequencies are well above the ones generated by the camshaft, but no conclusion can be drawn as this analysis still does not represent the operational conditions. This is because the spring during operation are allowed to rotate, the temperatures during operation is elevated, and some of the mass from other parts of the system will co-oscillate with the spring. The results from this analysis still gives an indication on the expected eigenfrequency range of the valve spring during operation.

The analysis performed on the spring at different temperatures indicate that the eigenfrequencies drops as the temperature is increased. This shows that the temperature does not have a huge impact, as the first eigenfrequencie drops from 503 Hz at 20 °C, to 496 Hz at 160 °C. The results are expected, as the Younges Modules of the material is decreasing with rising temperatures, hence reducing the stiffness of the spring. For the calculation of the changed material properties for increased temperatures, the behaviour of the library material ”Steel” in Siemens NX is used. It is not certain that the Si-CR-V-alloy behaves in the exact same way when exposed to elevated temperatures, but it is reasonable to assume that the results will be comparable for this material.

In order to take the extra mass from the other interacting parts into account, an analysis with additional mass oscillating with the spring was conducted. This analysis shows that by adding a mass in the range of 10-40 g to the top of the spring, resonance in the spring is possible during operation, as the eigenfrequencies are shifted all the way down to 50 Hz for an added mass of 40 g. In order to run this analysis, the spring is not constrained at the top, something that will have a great impact on the results. Therefore, the exact frequencies obtained should not be considered, but rather the fact that taking the extra mass into account will have a considerable impact on the eigenfrequencies of the spring.

From the dynamic analysis conducted in FEDEM, the eigenfrequencies of the system during operation is extracted. The system modes relevant for the spring are investigated and shows eigenfrequencies at 497 Hz and 572 Hz at the point of the cycle where the eigenfrequencies are at the lowest. This is still multiple times higher than the excitation frequency of 121 Hz imposed by the engine at max RPM. As it is not possible to simulate the coils intersecting during compression in FEDEM, the real stiffness of the spring can be assumed to be greater than the stiffness used for the eigenfrequency calculations at max compression. How much this increased stiffness would impact the result is not established, but it would further increase the eigenfrequenices of the spring, weakening the original hypothesis of resonance in the spring during operation.

The stress analysis in Siemens NX shows that the stress levels in the spring highly vary

over the different coils of the spring. The middle coils have the highest stress levels, and the maximal stress occur on the inner part of the coils. This is expected from looking at the spring theory. Here, the stress can reach a level of 1648 MPa when the spring is fully compressed, showing the very high stress condition in which the valve springs operate.

The fatigue analysis shows that fatigue could be a problem when the springs are approaching a very high number of cycles. Based on fatigue data obtained from studies on valve springs made of the same material, the analysis using the Goodman curve shows that for a service life of $N = 1.2 \times 10^9$ cycles there is a failure probability of more than 10%. For a service life of $N = 10^7$ cycles however, fatigue should not be a problem. For valve springs mounted in an engine running at high RPM, such as the ones of the Honda CRF 250R, a fatigue life of $N = 10^7$ cycles is not sufficient, as this only corresponds to constantly revving the engine at max RPM for approximately 24 hours. Even though this is not a representative loading situation, it indicates that a fatigue life of this level would not be sufficient, as the valve springs would need to be replaced often. In the case of very high cycle fatigue, with a fatigue life of $N = 1.2 \times 10^9$ cycles, the same scenario would yield approximately 2857 hours of service life before failure, something that would be acceptable. As the expected fatigue life is somewhere between these two limits, it can not be concluded whether fatigue is the problem on the basis of this analysis.

From the fatigue analysis in FEDEM, a service life of $N = 1.94 \times 10^{10}$ cycles seems to be possible, much longer than the one estimated using Goodman curves. The reason for this is that the stress level used in this analysis is lower than the one obtained from the simulation in Siemens NX, resulting in a longer fatigue life. Again, as the strain rosette is mounted at the middle coils of the spring, the stress levels are not representative for the areas of crack initiation in the actual failed spring.

Finally, these analyses are performed with the stress levels of the mid coils, whereas the reported failures in the valve springs of the Honda CRF 205R tend to happen in the end coils. The reason why the failures happens in these areas, even though the stress is significantly lower here, might be due to various types of stress concentration factors that could be present in the end coils. This could for example be a result of small scratches in the surface of the end coil generated during installation.

## 6.1 Conclusion

The dynamic analysis in FEDEM suggests that the spring during operation is well outside the range of frequencies causing resonance in the spring. As this simulation does not take the spring stiffening effect of the end coils coming in contact into account, and the total compression of the spring is slightly smaller than during operation, this should not be excluded as the reason for failure. However, it is a good indication that the problem might be due to other factors.

From the fatigue analysis it can be concluded that very high cycle fatigue could be possible

in the middle coils. The stress levels of the part of the spring where the springs actually fail however, are well bellow the fatigue limit of the material. Therefore, stress concentration factors have to be present in order for fatigue to be the problem in the end coils.

## 6.2 Further Work

Further work involve performing physical experiments on the actual valve springs of the Honda CRF 250R. By running a full scale test on the springs, the actual fatigue life can be established. In order to evaluate whether any of the named problems related to the valve springs are present during operation, it should be investigated how the springs behave in the actual engine during operation at different engine speeds.

To establish the exact fatigue life of the valve springs, physical tests should be conducted with the springs in question for the given operation cycle of the springs. Finally, the fracture surfaces of the failed springs should be investigated by the use of SEM in order to determine the fracture initiation sites, and if the reason for fracture is due to fatigue.

# Bibliography

B.Pyttela, I.Brunnera, B.Kaisera, C.Bergera, M.Mahendranb, 2014. Fatigue behaviour of helical compression springs at a very high number of cycles – investigation of various influences. International Journal of Fatigue 60 (-), 101–109.

CARDONA, A., LENS, E., NIGRO, N., 2002. Optimal design of cams. Multibody System Dynamics 7 (-), 285–305.

C.Berger, B.Kaiser, 2006. Results of very high cycle fatigue tests on helical compression springs. International Journal of Fatigue 28 (11), 1658–1663.

Compass ASTM, 2019. Standard astm a877/a877m. https://compass.astm.org/EDIT/html_annot.cgi?A877+17#s00027, Accessed: 6-5-2019.

de Bortoli, M. G. D., , Jr, R. B., Puff, R., 2010. Fatigue analysis of helical suspension springs for reciprocating compressors. International Compressor Engineering Conference - (1989), –.

Ding, K., Ye, L., 2006. Laser Shock Peening. Woodhead Publishing Limited.

DNV GL AS, 2016. Fatigue design of offshore steel structures. DNV GL AS.

Engineering, 2019. Spring info. http://engg-learning.blogspot.com/2011/03/helical-spring.html, Accessed: 15-4-2019.

Fedem Technology AS, 2016a. FEDEM Theroy guide. Fedem Technology AS.

Fedem Technology AS, 2016b. FEDEM user's guide. Fedem Technology AS.

Gavin, H. P., 2012. Mathematical properties of stiffness matrices. http://people.duke.edu/~hpgavin/cee421/matrix.pdf, Accessed: 11-10-2018.

Geehan, J. A. M., Ryason, P. R., 2000. Preventing catastrophic camshaft lobe failures in low emission diesel engines. SAE, Transactions Journal of Fuels and Lubricants 109 (4), 27.

Henderson, T., 2018a. Natural frequency. https://www.physicsclassroom.com/class/sound/Lesson-4/Natural-Frequency, Accessed: 28-10-2018.

Henderson, T., 2018b. Resonance. https://www.physicsclassroom.com/class/sound/Lesson-5/Resonance, Accessed: 28-10-2018.

Honda Motor Company, 2018. Honda CRF250R features. https://powersports.honda.com/2018/crf250r.aspx#features, Accessed: 11-09-2018.

It Still Runs, 2018. Valve spring assembly. https://s3.amazonaws.com/cme_public_images/www_ehow_com/i.ehow.com/images/a02/0d/5m/replace-valve-seals-engine-1.2-800x800.jpg, Accessed: 25-9-2018.

Jindal, U., 2010. Machine Design. Dorling Kindersley.

Jr., W. D. C., Rethwisch, D. G., 2000. Fundamentals of Materials Science and Engineering: An Integrated Approach, 4th Edition. Wiley.

Mechadyne International Limited, 2006. The impact of vale events upon engine performance and emissions. Mechadyne International Limited.

Rios, 2018. Valve timing. https://en.wikipedia.org/wiki/Valve_timing#/media/File:Valve_timing_4T.png, Accessed: 25-10-2018.

Roylance, P. D., 2001. Fatigue. Department of Materials Science and Engineering, Massachusetts Institute of Technology.

Rui-Ming, F., Ji-Fei, C., Guang, L., 2013. Cam curve synthesis method based on classical splines. Applied Mechanics and Materials 312 (-), 69–73.

Sahu, L. K., Kedia, V. K., Sahu, M., 2016. Design of cam and follower system using basic and synthetic curves: A review. IJISET 3 (2), 363–372.

Siemens AG, 2011. NX Nastran Advanced Nonlinear – Solution 601/701. Siemens AG.

Siemens AG, 2014a. Basic Dynamics NX. Siemens AG.

Siemens AG, 2014b. Element Library Reference. Siemens AG.

Siemens AG, 2019. Finite element analysis. https://www.plm.automation.siemens.com/global/en/our-story/glossary/finite-element-analysis-fea/13173, Accessed: 29-4-2019.

Sudhakar, K., 2001. Failure analysis of an automobile valve spring. Engineering Failure Analysis 8 (-), 513–520.

RØLVÅG, T., 2018. Tmm4155 - anvendelse av elementmetoden i maskinkonstruksjon. https://www.ntnu.no/studier/emner/TMM4155#tab=omEmnet, Accessed: 16-4-2019.

Vectorstock, 2018. Four stroke engine cycles. https://www.vectorstock.com/royalty-free-vector/four-stroke-engine-vector-20120974, Accessed: 16-10-2018.

Vizard, D., 1991. How to Build and Modify Chevrolet Small-Block V-8 Cylinder Heads. Motorbooks international.

Wang, W.-Y., Liu, B., Kodur, V., 2013. Effect of temperature on strength and elastic modulus of high-strength steel. American Society of Civil Engineers 25 (2), –.

ÇINAR, C., AKGÜN, F., 2007. Effect of intake valve closing time on engine performance and exhaust emissions in a spark ignition engine. Journal of Polytechnic 10 (4), 371–375.

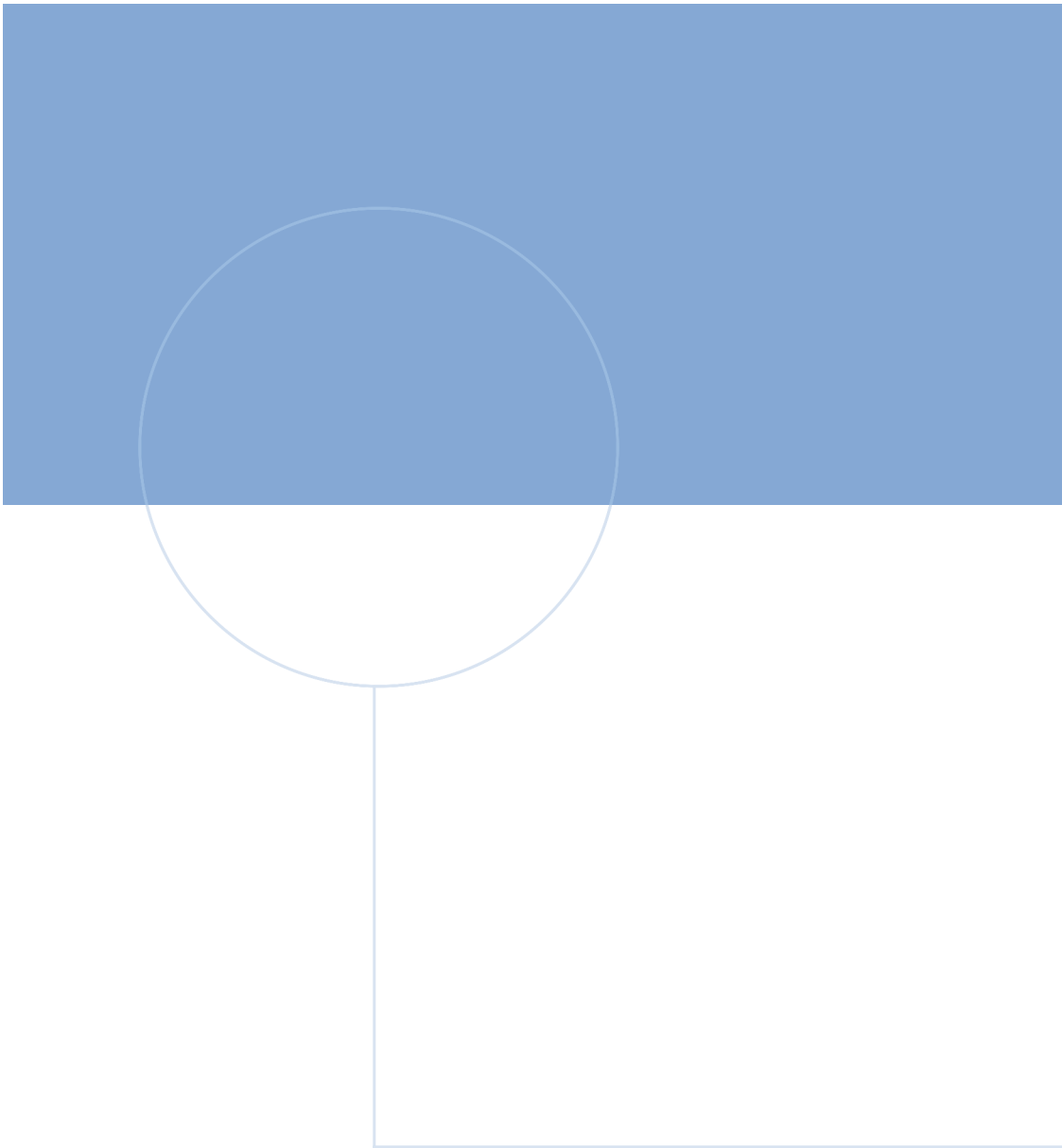

NTNU

Kunnskap for en bedre verden